

Arctic Sea Ice Reemergence: The Role of Large-Scale Oceanic and Atmospheric Variability*

MITCHELL BUSHUK, DIMITRIOS GIANNAKIS, AND ANDREW J. MAJDA

Courant Institute of Mathematical Sciences, New York University, New York, New York

(Manuscript received 21 May 2014, in final form 25 January 2015)

ABSTRACT

Arctic sea ice reemergence is a phenomenon in which spring sea ice anomalies are positively correlated with fall anomalies, despite a loss of correlation over the intervening summer months. This work employs a novel data analysis algorithm for high-dimensional multivariate datasets, coupled nonlinear Laplacian spectral analysis (NLSA), to investigate the regional and temporal aspects of this reemergence phenomenon. Coupled NLSA modes of variability of sea ice concentration (SIC), sea surface temperature (SST), and sea level pressure (SLP) are studied in the Arctic sector of a comprehensive climate model and in observations. It is found that low-dimensional families of NLSA modes are able to efficiently reproduce the prominent lagged correlation features of the raw sea ice data. In both the model and observations, these families provide an SST–sea ice reemergence mechanism, in which melt season (spring) sea ice anomalies are imprinted as SST anomalies and stored over the summer months, allowing for sea ice anomalies of the same sign to reappear in the growth season (fall). The ice anomalies of each family exhibit clear phase relationships between the Barents–Kara Seas, the Labrador Sea, and the Bering Sea, three regions that compose the majority of Arctic sea ice variability. These regional phase relationships in sea ice have a natural explanation via the SLP patterns of each family, which closely resemble the Arctic Oscillation and the Arctic dipole anomaly. These SLP patterns, along with their associated geostrophic winds and surface air temperature advection, provide a large-scale teleconnection between different regions of sea ice variability. Moreover, the SLP patterns suggest another plausible ice reemergence mechanism, via their winter-to-winter regime persistence.

1. Introduction

Arctic sea ice is a sensitive component of the climate system, with dynamics and variability that are strongly coupled to the atmosphere and ocean. This sensitivity is evident in the recent precipitous decline in September sea ice extent, of roughly 9% per decade since 1979 (Stroeve et al. 2007; Serreze et al. 2007). Trends in sea ice extent are negative for all months of the year and all Arctic regions except for the Bering Sea (Cavalieri and

Parkinson 2012). In addition to these strong trends, Arctic sea ice also exhibits large internal variability. Studies using comprehensive climate models have estimated that 50%–60% of recent Arctic sea ice changes can be attributed to externally forced trends, with the remainder resulting from internal variability in the climate system (Kay et al. 2011; Stroeve et al. 2012). Therefore, the challenge of making accurate projections of future Arctic sea ice conditions crucially hinges on 1) quantifying the sea ice response to changes in external forcing (i.e., greenhouse gas forcing) and 2) understanding the nature and magnitude of internal variability in the coupled ice–ocean–atmosphere system. This study will focus on the latter.

The Arctic regions of interest in this study are shown in Fig. 1. The leading empirical orthogonal function (EOF) of observational Arctic sea ice concentration (SIC) exhibits strong out-of-phase anomalies between the Labrador and Greenland–Barents Seas and weaker out-of-phase anomalies between the Bering Sea and Sea of Okhotsk (Deser et al. 2000). Regression of sea level

 Denotes Open Access content.

* Supplemental information related to this paper is available at the Journals Online website: <http://dx.doi.org/10.1175/JCLI-D-14-00354.s1>.

Corresponding author address: Mitch Bushuk, Center for Atmosphere Ocean Science, Courant Institute of Mathematical Sciences, New York University, 251 Mercer Street, New York, NY 10012.
E-mail: bushuk@cims.nyu.edu

DOI: JCLI-D-14-0/JCLI-D-14-00354.1

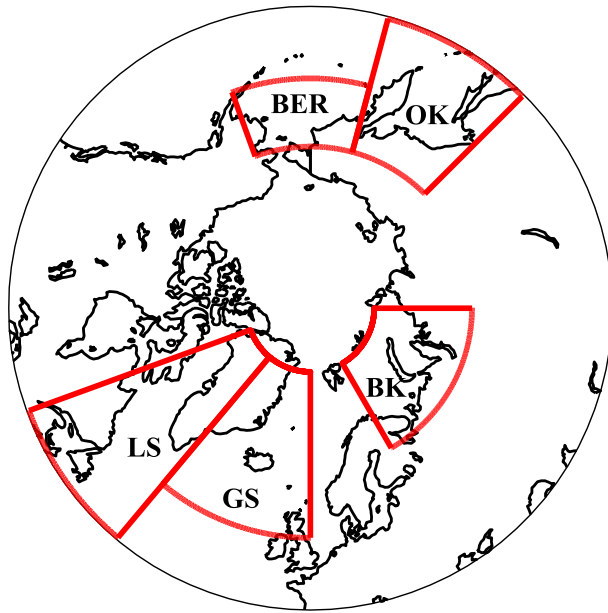


FIG. 1. The regions of interest in this study: the Barents–Kara Seas (BK), the Labrador Sea (LS), the Greenland Sea (GS), the Bering Sea (BER), and the Sea of Okhotsk (OK). The Arctic domain is defined as all grid points north of 45°N.

pressure (SLP) onto the corresponding principal component (PC) yields a spatial pattern that closely resembles the Arctic Oscillation (AO; [Thompson and Wallace 1998](#)), the leading pattern of SLP variability north of 20°N. [Deser et al. \(2000\)](#) observe a connection between the low-frequency (interannual to decadal) variability of the atmosphere and the low-frequency variability of sea ice. In particular, they find that the AO and its associated geostrophic winds are physically consistent with the ice anomalies of the leading SIC mode, suggesting that atmospheric circulation anomalies force sea ice anomalies. These winds have thermodynamic and dynamic effects on sea ice via advection of surface air temperature and ice advection. Many other studies have analyzed sea ice variability in the context of the AO, finding that the AO affects sea ice on a wide range of time scales ranging from seasonal ([Serreze et al. 2003](#)) to decadal ([Rigor et al. 2002](#); [Rigor and Wallace 2004](#); [Zhang et al. 2004](#)). These studies suggest that a “high index” AO produces an Ekman divergence, leading to reductions in sea ice thickness and concentration. This process has been proposed as a mechanism for the recent decline in Arctic sea ice.

Others have questioned the efficacy of the AO as a predictor for sea ice changes ([Maslanik et al. 2007](#)), suggesting that other patterns of large-scale atmospheric variability may play a more important role. In particular, an SLP pattern known as the Arctic dipole anomaly (DA) has drawn considerable recent attention ([Wu et al.](#)

[2006](#); [Wang et al. 2009](#); [Tsukernik et al. 2010](#); [Overland and Wang 2005, 2010](#); [Watanabe et al. 2006](#)). The DA exhibits opposite-signed SLP anomalies between the eastern and western Arctic, which drive strong meridional winds. These winds act to enhance (reduce) sea ice export from the Arctic basin through Fram Strait when the DA is in positive (negative) phase. Recent record lows in summer sea ice extent generally correspond to years in which the DA index was positive ([Wang et al. 2009](#)). DA-like SLP patterns have also been associated with the large internal variability observed in the sea ice component of the Community Climate System Model, version 3 (CCSM3; [Collins et al. 2006](#); [Wettstein and Deser 2014](#)). Other studies have suggested that the location and frequency of storms ([Screen et al. 2011](#)), and the phase of the Pacific–North America (PNA) pattern ([L’Heureux et al. 2008](#)) also play an important role in setting the summer sea ice minimum.

The PCs corresponding to large-scale atmospheric patterns, such as the AO and DA, are quite noisy and contain significant spectral power at time scales ranging from monthly to decadal. A typical approach has been to initially low-pass filter the atmospheric component (by forming annual or winter means), as a way of smoothing out these PCs and emphasizing interannual to decadal variability. Besides the studies already cited, a large number of works have analyzed the impact of this low-frequency atmospheric variability on Arctic sea ice ([Walsh et al. 1996](#); [Proshutinsky and Johnson 1997](#); [Mysak and Venegas 1998](#); [Yi et al. 1999](#); [Johnson et al. 1999](#); [Deser et al. 2000](#); [Polyakov and Johnson 2000](#); [Moritz et al. 2002](#)). These studies emphasize that sea ice regimes are modulated by low-frequency atmospheric circulation regimes.

The variability of Arctic sea ice is also strongly coupled to sea surface temperature (SST) variability (e.g., [Francis and Hunter 2007](#)). [Blanchard-Wrigglesworth et al. \(2011\)](#) proposed a mechanism for sea ice–SST covariability, in which sea ice and SST anomalies trade off, allowing for unexpected “memory” effects in sea ice. These memory effects were termed “sea ice reemergence,” inspired by the similar North Pacific and North Atlantic SST phenomena ([Alexander et al. 1999](#); [Timlin et al. 2002](#); [de Coëtlogon and Frankignoul 2003](#)). Sea ice reemergence is a lagged correlation phenomenon, in which spring sea ice anomalies are positively correlated with fall sea ice anomalies, despite a loss of correlation over the intervening summer months. There is also a similar, but weaker, reemergence between fall sea ice anomalies and anomalies the following spring. The spring–fall mechanism of [Blanchard-Wrigglesworth et al. \(2011\)](#) suggests that spring sea ice anomalies imprint SST anomalies of opposite sign, which persist

over the summer months. During the fall, ice grows southward and interacts with these SST anomalies, reproducing ice anomalies of the same sign as the spring. This reemergence mechanism has been observed in the North Pacific sector in the CCSM3 model output and observations (Bushuk et al. 2014). Deser et al. (2002) note a similar winter-to-winter persistence of sea ice anomalies in the Labrador Sea and propose an atmospheric mechanism in which sea ice anomalies persist because of persistent large-scale atmospheric circulation regimes.

Sea ice reemergence may also have implications for sea ice predictability. Day et al. (2014) found that sea ice forecast skill was strongly dependent on initialization month, with certain months exhibiting a slower decay of forecast skill than others. The authors suggested that this initialization month dependence was attributable to sea ice reemergence mechanisms. Day et al. (2014) also examined sea ice reemergence in five global climate models (GCMs) and observations, finding robust reemergence signals, of varying strength, across all models and a weaker reemergence signal in the observational record.

In this study, we examine the coupled variability of Arctic SIC, SST, and SLP using nonlinear Laplacian spectral analysis (NLSA), a recently developed data analysis technique for high-dimensional nonlinear time series (Giannakis and Majda 2012a,b, 2013, 2014). The NLSA algorithm is a nonlinear manifold generalization of singular spectrum analysis (SSA; Broomhead and King 1986; Vautard and Ghil 1989; Ghil et al. 2002). SSA is also commonly referred to as extended empirical orthogonal function (EEOF) analysis. Here, we apply the multivariate version of the NLSA algorithm, coupled NLSA (Bushuk et al. 2014), which provides a scale-invariant analysis of multiple variables with different physical units. Coupled NLSA yields spatiotemporal modes, analogous to EEOFs, and temporal modes, analogous to PCs. These modes are constructed using a set of empirically derived Laplacian eigenfunctions on the nonlinear data manifold and, unlike linear approaches, do not maximize explained variance. Compared to linear techniques, NLSA (and other related nonlinear methods; Berry et al. 2013) provides superior time-scale separation and is able to effectively capture low-variance modes that may have important dynamical significance. These low-variance modes are known to be crucial in producing accurate representations of nonlinear dynamical systems (Aubry et al. 1993; Giannakis and Majda 2012b) and, in the present context, are efficient in explaining reemergence phenomena (Bushuk et al. 2014).

We use coupled NLSA modes to study the basinwide and regional characteristics of Arctic sea ice reemergence in a comprehensive climate model and observations. We compute modes using CCSM3 model

output from a 900-yr equilibrated control integration. Modes are also obtained for the 34-yr observational record, using SIC and SST data from the Met Office Hadley Centre Sea Ice and Sea Surface Temperature dataset (HadISST) and the European Centre for Medium-Range Weather Forecasts (ECMWF) Interim Re-Analysis (ERA-Interim) SLP data. No preprocessing of the data is required, enabling simultaneous extraction of interannual, annual, and semiannual patterns of variability. Using these modes, we identify low-dimensional families that efficiently describe sea ice reemergence. These families capture a significant portion of the reemergence signal, and have the surprising property of being relatively low variance. The families also reveal time-dependent aspects of reemergence, which were not accessible in previous studies. The SST and SIC modes of each family exhibit an SST–sea ice reemergence mechanism consistent with that of Blanchard-Wrigglesworth et al. (2011). Interannual components of large-scale SLP variability, which emerge objectively from this analysis, are found to be related to coherent sea ice reemergence events in geographically distinct regions and suggest an SLP–sea ice reemergence mechanism.

This paper is organized as follows: In section 2, we summarize the coupled NLSA algorithm. In section 3, we describe the CCSM3, HadISST, and ERA-Interim datasets used in this study. In section 4, we study the SIC, SST, and SLP spatiotemporal modes obtained via coupled NLSA. In section 5, we examine the regional and temporal characteristics of sea ice reemergence, and in section 6 we investigate oceanic and atmospheric reemergence mechanisms. We conclude in section 7. (Movies, illustrating the spatiotemporal evolution of NLSA modes, are available as supplemental material at the Journals Online website: <http://dx.doi.org/10.1175/JCLI-D-14-00354.s1>.)

2. Coupled NLSA methodology

In this study, we apply the coupled NLSA approach, as developed in Bushuk et al. (2014), to Arctic SIC, SST, and SLP. This technique is an extension of the recently developed NLSA algorithm (Giannakis and Majda 2012b, 2013) and provides a scale-invariant approach for multivariate time series analysis. Unlike other multivariate data analysis approaches, coupled NLSA does not require initial normalization of the input fields to unit variance. Rather, the coupled NLSA algorithm implicitly selects the variance ratio between different physical fields, without requiring a choice of normalization by the user. Here, we briefly summarize the method and refer the reader to the more thorough description of Bushuk et al. (2014). Figure 2 is a schematic that summarizes the flow of data in the coupled NLSA algorithm.

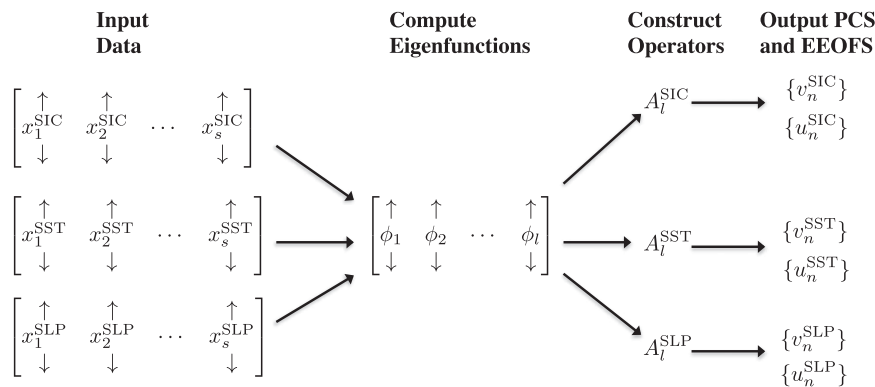


FIG. 2. Schematic summarizing the flow of data in the coupled NLSA algorithm.

Let x_t^{SIC} , x_t^{SST} , and x_t^{SLP} be time series for SIC, SST, and SLP, respectively, each sampled uniformly at time step δt , with s time samples. The dimensions of x_t^{SIC} , x_t^{SST} , and x_t^{SLP} are d_{SIC} , d_{SST} , and d_{SLP} , respectively, which are the number of spatial grid points for each variable. First, we choose a time lag window $\Delta t = q\delta t$ and time-lag embed our data into the higher-dimensional spaces $\mathbb{R}^{d_{\text{SIC}}q}$, $\mathbb{R}^{d_{\text{SST}}q}$, and $\mathbb{R}^{d_{\text{SLP}}q}$. Time-lagged embedding is performed via the delay-coordinate mappings,

$$x_t^{\text{SIC}} \mapsto X_t^{\text{SIC}} = (x_t^{\text{SIC}}, x_{t-\delta t}^{\text{SIC}}, \dots, x_{t-(q-1)\delta t}^{\text{SIC}}),$$

$$x_t^{\text{SST}} \mapsto X_t^{\text{SST}} = (x_t^{\text{SST}}, x_{t-\delta t}^{\text{SST}}, \dots, x_{t-(q-1)\delta t}^{\text{SST}}), \quad \text{and}$$

$$x_t^{\text{SLP}} \mapsto X_t^{\text{SLP}} = (x_t^{\text{SLP}}, x_{t-\delta t}^{\text{SLP}}, \dots, x_{t-(q-1)\delta t}^{\text{SLP}}).$$

The coupled NLSA approach uses these time-lagged-embedded data to construct a set of orthonormal basis functions on the nonlinear data manifold. These basis functions are eigenfunctions of a discrete Laplacian operator and are computed using a kernel (similarity) function defined through the physical variables of interest, as determined by the user of the algorithm. The kernel and corresponding Laplacian eigenfunctions can be thought of as nonlinear analogs of the covariance matrix and corresponding PCs of SSA, respectively. In this work, the kernel function values K_{ij} is an exponentially decaying similarity function constructed using SIC, SST, and SLP: namely,

$$K_{ij} = \exp\left(-\frac{\|X_i^{\text{SIC}} - X_j^{\text{SIC}}\|^2}{\epsilon \|\xi_i^{\text{SIC}}\| \|\xi_j^{\text{SIC}}\|} - \frac{\|X_i^{\text{SST}} - X_j^{\text{SST}}\|^2}{\epsilon \|\xi_i^{\text{SST}}\| \|\xi_j^{\text{SST}}\|} - \frac{\|X_i^{\text{SLP}} - X_j^{\text{SLP}}\|^2}{\epsilon \|\xi_i^{\text{SLP}}\| \|\xi_j^{\text{SLP}}\|}\right),$$

where $i, j \in [q+1, q+2, \dots, s]$. Here, ϵ is a scale parameter controlling the width of the Gaussian, and

$\xi_i^k = X_i^k - X_{i-1}^k$ is the phase space velocity of the k th variable. Note that, because of the division by $\|\xi_i^k\|$, the argument of the exponential is unit independent, allowing for a natural comparison of the different variables in the system. Performing an appropriate normalization, we convert the kernel matrix \mathbf{K} to a Laplacian matrix \mathbf{L} and solve the eigenvalue problem

$$\mathbf{L}\phi_i = \lambda_i\phi_i.$$

This yields a set of discrete Laplacian eigenfunctions $\{\phi_1, \phi_2, \dots, \phi_{s-q}\}$: each of which is a temporal pattern of length $s - q$. By virtue of the delay-coordinate mapping of the data, these patterns are conditioned to reveal intrinsic dynamical time scales in the data, such as those associated with quasi-periodic orbits (Berry et al. 2013). In practice only $l \ll s$ of these eigenfunctions are used and need to be computed. The eigenfunctions are used as a temporal filter for the data, analogous to Fourier modes, but intrinsic to the dynamical system generating the data.

Let Φ_l be the matrix whose columns consist of the leading l eigenfunctions. Let $\mathbf{X}^k: \mathbb{R}^{s-q} \mapsto \mathbb{R}^{qd_k}$ be the lag-embedded data matrix for the k th variable,

$$\mathbf{X}^k = \begin{bmatrix} X_{q+1}^k & X_{q+2}^k & \dots & X_s^k \end{bmatrix}.$$

Projecting \mathbf{X}^k onto the leading l Laplacian eigenfunctions, we construct linear maps $\mathbf{A}_l^k: \mathbb{R}^l \mapsto \mathbb{R}^{qd_k}$, given by

$$\mathbf{A}_l^k = \mathbf{X}^k \boldsymbol{\mu} \Phi_l. \quad (1)$$

Here μ_i is the i th entry of the stationary distribution of the Markov chain corresponding to \mathbf{K} , and $\boldsymbol{\mu}$ is a diagonal matrix with μ_i along the diagonal. Note that the variables used to construct the eigenfunctions do not necessarily need to coincide with the variables for which we compute the \mathbf{A}_l^k operators. For example, we can use

the SIC–SST–SLP eigenfunctions to filter any other variable of interest in our system.

Singular value decomposition (SVD) of the operator for the k th variable \mathbf{A}_l^k yields a set of spatiotemporal modes $\{u_n^k\}$ of dimension qd_k , analogous to EEOFs, and a corresponding set of length l vectors $\{V_n^k\}$. These $\{V_n^k\}$ are the expansion coefficients in eigenfunction basis. Expanding using the first l eigenfunctions, we recover a set of temporal modes $\{v_n^k\}$ of length $s - q$, where $v_n^k = \Phi_l V_n^k$. These modes, indexed by n , are ordered by decreasing singular value σ_n^k . Forming products $u_n^k \sigma_n^k (v_n^k)^T$ and projecting from lagged-embedding space to physical space using the standard approach (Ghil et al. 2002), we obtain reconstructed fields $\hat{u}_n^k(t)$.

3. Dataset description

a. CCSM3 model output

This study analyzes model output from a 900-yr equilibrated control integration (model run b30.004) of CCSM3 (Collins et al. 2006). These data were downloaded from the Earth System Grid website. We use monthly averaged data for SIC, SST, and SLP, which come from the Community Sea Ice Model (CSIM; Holland et al. 2006); the Parallel Ocean Program (POP; Smith and Gent 2004); and the Community Atmosphere Model, version 3 (CAM3; Collins et al. 2004), respectively. The model uses a T42 spectral truncation for the atmospheric grid (roughly $2.8^\circ \times 2.8^\circ$), and the ocean and sea ice variables are defined on the same grid, of 1° nominal resolution. This study focuses on a pan-Arctic domain, which we define as all grid points north of 45°N . Note that the seasonal cycle has not been removed from this dataset. This is crucial for capturing intermittent patterns associated with reemergence. In particular, intermittent modes, described in section 4, are not recoverable in datasets that have been deseasonalized (Giannakis and Majda 2013). As will be shown in section 5, these modes are essential in low-dimensional descriptions of sea ice reemergence.

The spatial dimensions (number of spatial grid points) of these datasets are $d_{\text{SIC}} = d_{\text{SST}} = 13\,202$ and $d_{\text{SLP}} = 2048$. Using a 2-yr embedding window with $q = 24$ (Giannakis and Majda 2012b; Bushuk et al. 2014), this yields lagged-embedding dimensions (the product of the number of spatial grid points and the embedding window) of $qd_{\text{SIC}} = qd_{\text{SST}} = 316\,848$ and $qd_{\text{SLP}} = 49\,152$. These data are monthly averaged and consist of $s = 10\,800$ time samples for the 900-yr simulation period. The value $\Delta t = 24$ months was used as the time lag because this embedding window is longer than the seasonal cycle, which is a primary source of non-Markovianity in

this dataset. A number of different embedding windows were tested, yielding qualitatively similar results for $\Delta t \geq 12$ months and qualitatively different results for $\Delta t < 12$ months.

b. HadISST observations

We also analyze HadISST (Rayner et al. 2003), which consists of monthly averaged SIC and SST data on a 1° latitude–longitude grid. The spatial dimension of the Arctic domain is $d_{\text{SIC}} = d_{\text{SST}} = 9453$. As with the CCSM3 data, we use an embedding window of $\Delta t = 24$ months, which yields lagged-embedding dimensions of $qd_{\text{SIC}} = qd_{\text{SST}} = 226\,872$. In this study we use the satellite era data from January 1979 to August 2013. Note that all ice-covered grid points in HadISST were assigned an SST value of -1.8°C , the freezing point of saltwater at a salinity of 35 parts per thousand. Also, the trend in the dataset was removed by computing a long-term linear trend for each month of the year and removing the respective linear trend from each month. The seasonal cycle has not been removed from this dataset.

c. ERA-Interim data

Finally, we also study monthly averaged SLP data from ERA-Interim (Dee et al. 2011). These data are defined on a 0.75° latitude–longitude grid, of considerably higher resolution than the CCSM3 SLP data. The spatial dimension of the Arctic domain is $d_{\text{SLP}} = 29\,280$, corresponding to a lagged-embedding dimension of $qd_{\text{SLP}} = 702\,720$. These data have been detrended by subtracting the monthly trend from each month, but the seasonal cycle has not been subtracted.

4. Coupled SIC–SST–SLP spatiotemporal modes of Arctic variability

We utilize the coupled NLSA algorithm outlined in section 2 to study the spatiotemporal evolution of (i) SIC, SST, and SLP in CCSM3 and (ii) SIC and SST from HadISST and SLP from ERA-Interim. Hereafter, we refer to the joint HadISST and ERA-Interim datasets as observations. For both the model and observational data, we use a lagged-embedding window of $\Delta t = 24$ months.

a. CCSM3 modes

We choose ϵ , the Gaussian locality parameter, as $\epsilon = 0.90$. Using the spectral entropy criterion of Giannakis and Majda (2012a, 2013), we select a truncation level of $l = 27$ eigenfunctions and express the data matrices \mathbf{X}^{SIC} , \mathbf{X}^{SST} , and \mathbf{X}^{SLP} in this basis. SVD of the resulting operators [see Eq. (1)] yields a set of spatiotemporal patterns, $\{u_n^{\text{SIC}}\}$, $\{u_n^{\text{SST}}\}$, and $\{u_n^{\text{SLP}}\}$, and a set of temporal

patterns, $\{v_n^{\text{SIC}}\}$, $\{v_n^{\text{SST}}\}$, and $\{v_n^{\text{SLP}}\}$, for each variable. The modes are ordered by decreasing singular value. In general, the temporal patterns for different variables need not be related. However, by virtue of the relatively low dimensionality of the eigenfunction basis relative to the original temporal dimension ($l = 27 \ll s = 10800$) and, because the eigenfunctions incorporate information from all three variables, we find strong correlations between the temporal patterns of different variables.

1) TEMPORAL MODES

Figures 3–5 show selected temporal patterns for SIC, SST, and SLP, respectively. For each variable, we observe three distinct types of temporal modes: periodic, low-frequency, and intermittent modes, indicated by P , L , and I in the figures.

The periodic temporal modes closely resemble sinusoids, with frequencies given by integer multiples of 1 yr^{-1} . These modes appear as doubly degenerate pairs, with a phase offset of $\pi/2$. The leading periodic modes, representing the annual and semiannual cycles, capture more variance than the low-frequency and intermittent modes of the system. Higher harmonic periodic modes are found later in the mode spectrum. The low-frequency modes are characterized by significant interannual variability and have a typical decorrelation time of approximately 3 years. These modes carry significant spectral power at frequencies below 1 yr^{-1} and exhibit a sharp decline in spectral power at frequencies above this.

The intermittent modes are characterized by periods of intense activity followed by periods of quiescence. Each intermittent mode has a base frequency of oscillation and a broadband peak in spectral power centered upon this frequency. These modes carry lower variance than their periodic and low-frequency counterparts, yet they have potentially high dynamical significance. For example, annual and semiannual intermittent modes are crucial components in low-dimensional descriptions of sea ice reemergence phenomena (Bushuk et al. 2014). Note that the leading low-frequency and intermittent modes are insensitive to truncation level, whereas increasing l will eventually disrupt the temporal character of some intermittent modes.

Intermittent modes closely resemble a periodic signal modulated by a low-frequency envelope. We find that nearly all intermittent modes can be directly associated with a particular low-frequency mode, which provides this modulating envelope (Bushuk et al. 2014). To determine this association, we compare the envelope function of the intermittent modes to the low-frequency modes. We find the envelope function via the Hilbert transform (von Storch and Zwiers 1999). Let $I(t)$ be

a given intermittent mode and let $H(I)(t)$ be the Hilbert transform of I . Then the envelope function $e(t)$ is given by $e(t) = [I(t)^2 + H(I)(t)^2]^{1/2}$. Next, we determine which low-frequency mode provides this modulating envelope by performing a correlation between $e(t)$ and $|L(t)|$, where $L(t)$ is a low-frequency mode. Figure 6 shows these correlation values for intermittent and low-frequency modes of each variable, for both the model and observations. Note that the low-frequency–intermittent mode association is quite clear for most variables, except for the observational SLP, whose intermittent envelopes generally correlate weakly with the low-frequency modes.

As a comparison, we also performed SSA on the concatenated and unit-variance normalized SIC–SST–SLP dataset. Similar to the findings of Bushuk et al. (2014), SSA produces periodic modes, many low-frequency modes, and some modes that loosely resemble the intermittent modes of NLSA, with a spectral maximum at a certain base frequency. We find that the SSA modes do not share the same intermittent–low-frequency mode relationships as the NLSA modes. These relationships will be important for explaining reemergence, as they reflect the interaction of large-scale low-frequency modes of variability with the familiar annual and semiannual cycles in the climate system.

2) SIC SPATIOTEMPORAL PATTERNS

Figure 7 shows spatial patterns of selected modes at a snapshot in time. Movies 1 and 2 in the online supplementary material show the spatiotemporal evolution of these modes and others. Below, we describe the prominent features of the spatiotemporal modes recovered for SIC, SST, and SLP.

The annual periodic SIC modes $\{P_1^{\text{SIC}}, P_2^{\text{SIC}}\}$ (Fig. 7a) have spatially uniform anomalies throughout most of the Arctic, except at high-latitude grid points, where there is year-round ice coverage, and in the marginal ice zones, where the anomalies are slightly weaker. These anomalies reach their maximum and minimum values in March and September, respectively. The higher-frequency periodic modes have increasingly finer spatial structure and capture a decreasing portion of the variance.

The low-frequency modes closely resemble the leading EOFs of Arctic SIC in the CCSM3 model. Mode L_1^{SIC} (Fig. 7d) exhibits anomalies in the Bering, Beaufort, and Labrador Seas, which are out of phase with the anomalies of the Barents, Kara, and Greenland Seas. Computing pattern correlations between the q spatial patterns of L_1^{SIC} and the different EOFs of deseasonalized Arctic SIC, we find a maximum pattern correlation of 0.97 with EOF1. Mode L_2^{SIC} (Fig. 7g) has strong anomalies in the Bering and Labrador Seas, which are

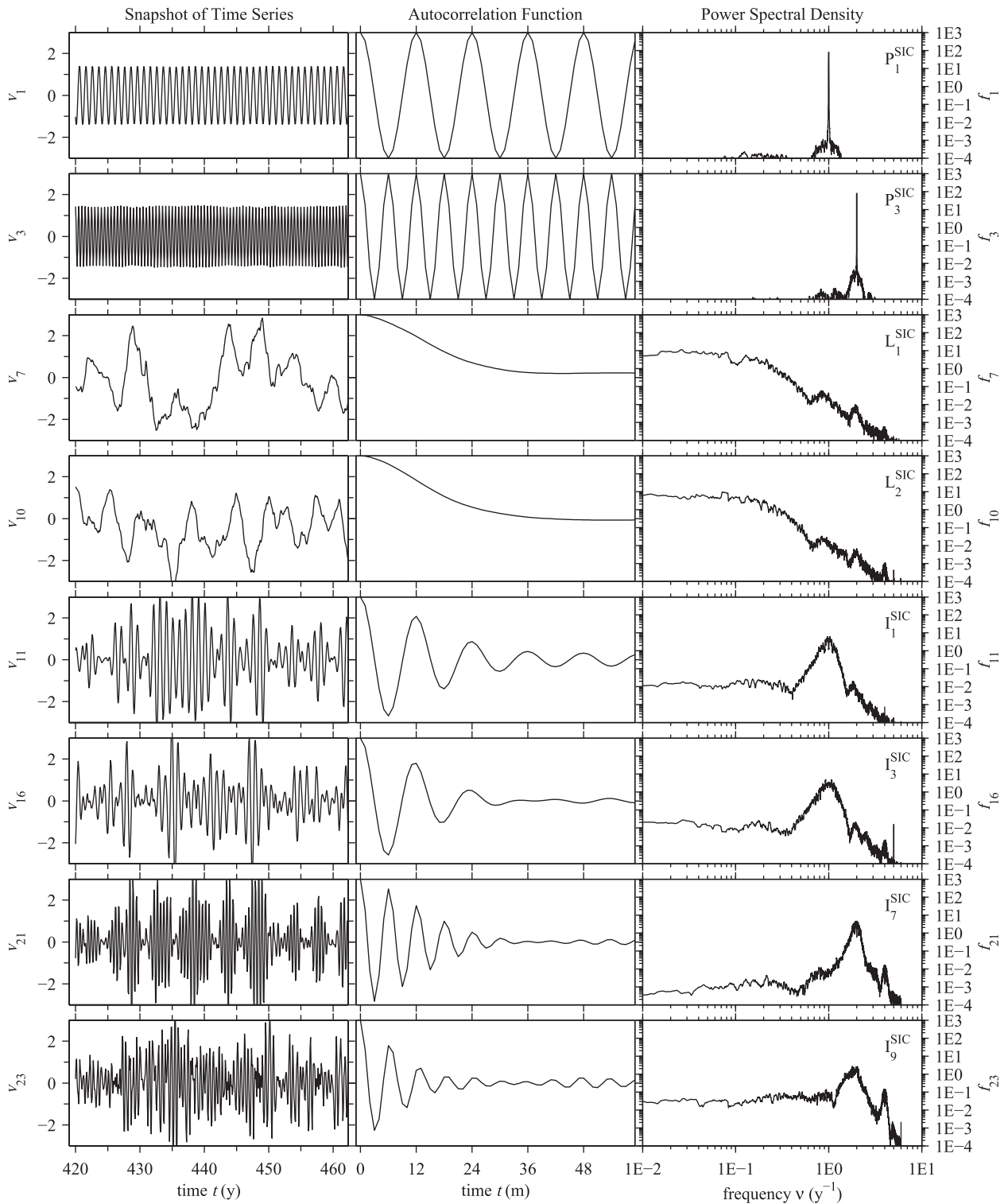


FIG. 3. Snapshots of the time series, power spectral density, and autocorrelation functions for the CCSM3 SIC PCs (v_k) from coupled NLSA. Shown here for 50-yr portions of the 900-yr time series are the annual periodic (p_1^{SIC}) and semiannual periodic (p_3^{SIC}) modes, low-frequency modes (L_1^{SIC} and L_2^{SIC}), annual intermittent modes (I_1^{SIC} and I_3^{SIC}), and semiannual intermittent modes (I_7^{SIC} and I_9^{SIC}). The autocorrelation vertical scale is $[-1, 1]$. The power spectral densities (f_k) were estimated via the multitaper method with time–bandwidth product $p = 6$ and $K = 2p - 1 = 11$ Slepian tapers. The effective half-bandwidth resolution for the s monthly samples is $\Delta\nu = p/(s\delta t) = 1/150 \text{ yr}^{-1}$, where $\delta t = 1/12 \text{ yr}$ is the sampling interval.

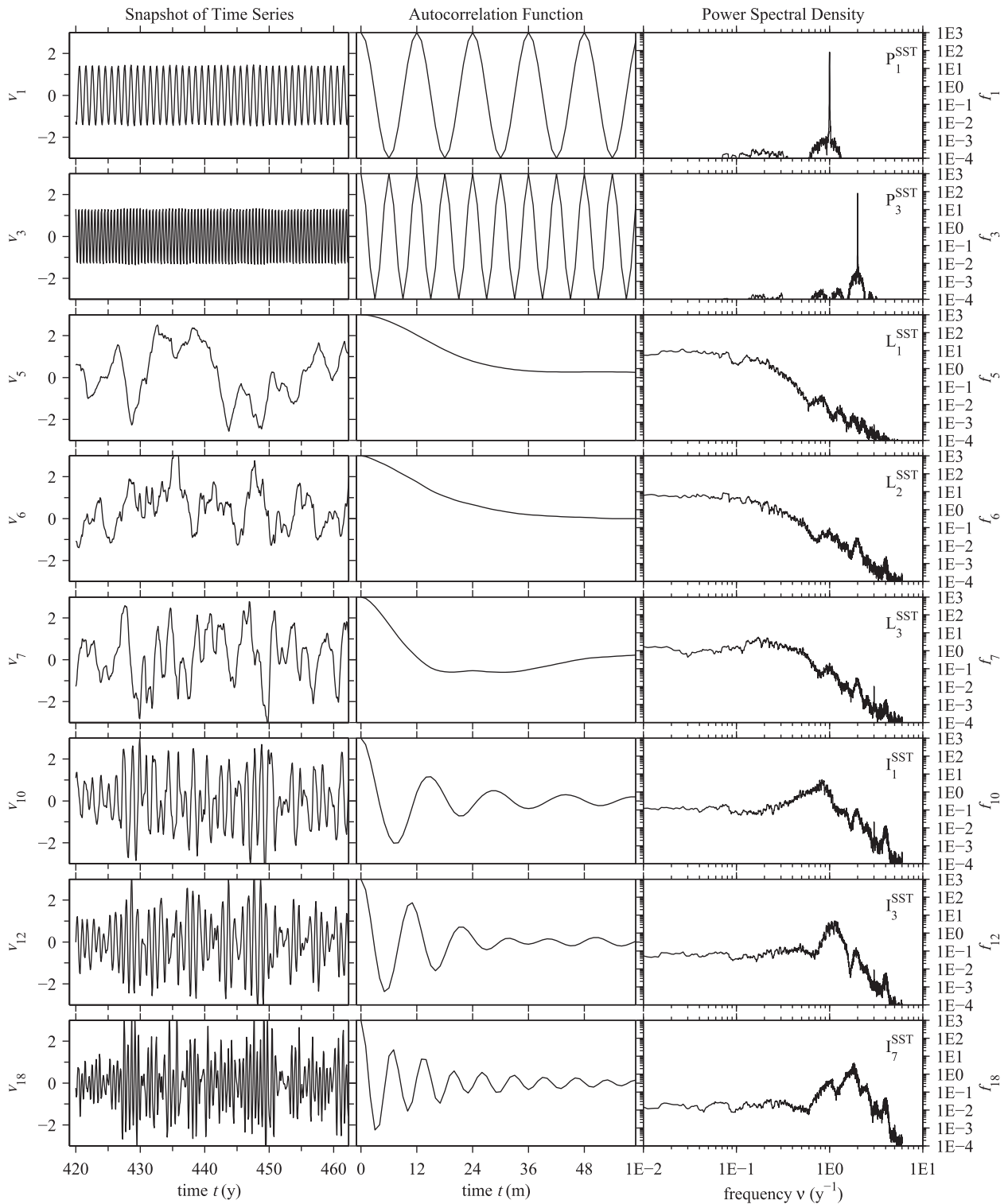


FIG. 4. Snapshots of the time series, power spectral density, and autocorrelation functions for the CCSM3 SST PCs from coupled NLSA. Shown here are the annual periodic (P_1^{SST}) and semiannual periodic (P_3^{SST}) modes, low-frequency modes (L_1^{SST} , L_2^{SST} , and L_3^{SST}), annual intermittent modes (I_1^{SST} and I_3^{SST}), and semiannual intermittent modes (I_7^{SST}). The autocorrelation vertical scale is $[-1, 1]$.

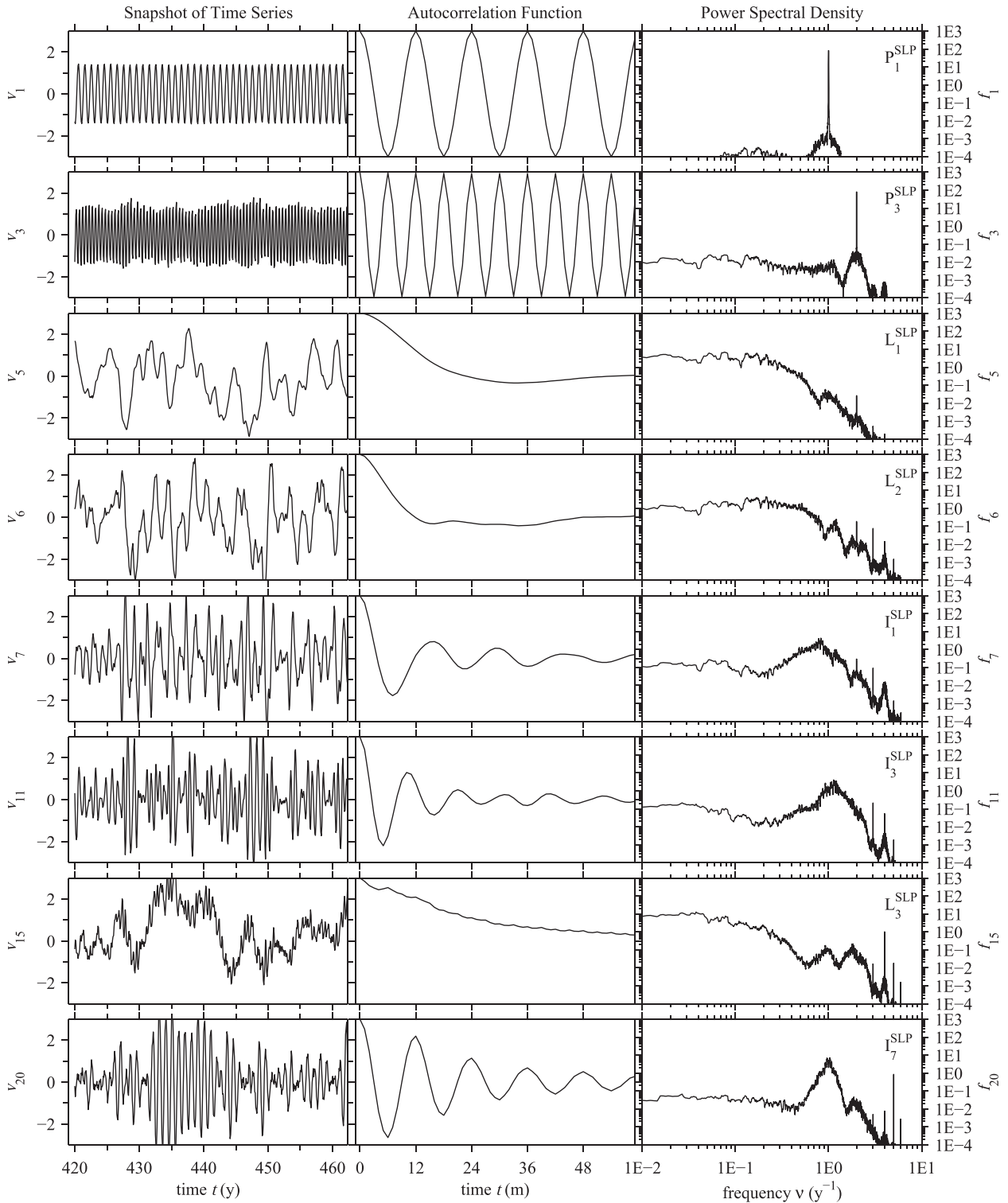


FIG. 5. Snapshots of the time series, power spectral density, and autocorrelation functions for the CCSM3 SLP PCs from coupled NLSA. Shown here are the annual periodic (P_1^{SLP}) and semiannual periodic (P_3^{SLP}) modes, low-frequency modes (L_1^{SLP} , L_2^{SLP} , and L_3^{SLP}), and intermittent modes (I_1^{SLP} , I_3^{SLP} , and I_7^{SLP}). The autocorrelation vertical scale is $[-1, 1]$.

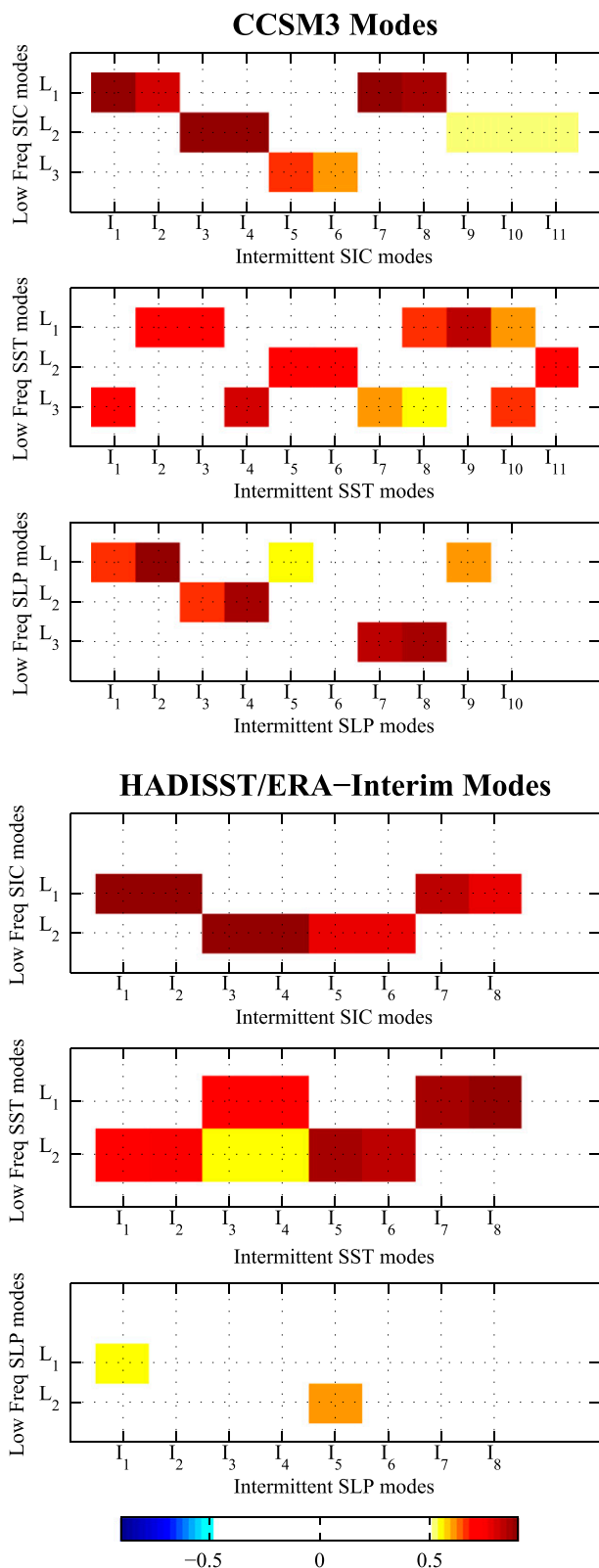


FIG. 6. Correlations between low-frequency modes and envelope functions for intermittent modes. Mode pairs with large positive correlations indicate that the low-frequency mode provides the modulating envelope for the intermittent mode.

out of phase with one another. It also has weaker anomalies in the Sea of Okhotsk, Barents Sea, and Kara Sea, which are in phase with the Bering Sea anomalies. This mode has a maximum pattern correlation of 0.77 with EOF3.

Each intermittent mode has a natural association with a certain low-frequency mode, which acts as a modulating envelope for the intermittent mode. There is also a clear spatial connection, as the intermittent modes are active in the same parts of the domain as their low-frequency counterpart. The annual and semiannual intermittent mode pairs $\{I_1^{\text{SIC}}, I_2^{\text{SIC}}\}$ and $\{I_7^{\text{SIC}}, I_8^{\text{SIC}}\}$ are associated with L_1^{SIC} (see Fig. 6). These modes pulse with annual and semiannual frequency, respectively, and exhibit finer spatial structure than L_1^{SIC} . In regions where L_1^{SIC} has monopole anomalies, these intermittent modes have dipole and tripole anomalies, respectively. The annual and semiannual intermittent modes $\{I_3^{\text{SIC}}, I_4^{\text{SIC}}\}$ and $\{I_9^{\text{SIC}}, I_{10}^{\text{SIC}}, I_{11}^{\text{SIC}}\}$ are associated with L_2^{SIC} and share similar spatial relationships.

3) SST SPATIOTEMPORAL PATTERNS

Mode L_1^{SST} (Fig. 7e) has strong anomalies in the Bering Sea that extend southward into the northeastern Pacific, and anomalies of the opposite sign in the Barents and Kara Seas. There is also a North Atlantic signal with anomalies in the subpolar gyre region that are in phase with the North Pacific anomalies. This mode has a maximum pattern correlation of 0.98 with EOF1 of Arctic SST from CCSM3. Mode L_2^{SST} (Fig. 7h) exhibits out-of-phase anomalies between the North Pacific and North Atlantic. The North Atlantic anomalies correspond to variability in the subpolar gyre, and the North Pacific anomalies are strongest in the Bering Sea, extending through most of the Pacific portion of the domain. This mode is most similar to EOF2, with 0.96 pattern correlation.

The intermittent modes associated with L_1^{SST} and L_2^{SST} are $\{I_1^{\text{SST}}, I_2^{\text{SST}}, I_8^{\text{SST}}, I_9^{\text{SST}}\}$ and $\{I_5^{\text{SST}}, I_6^{\text{SST}}, I_{11}^{\text{SST}}\}$, respectively. As with the SIC modes, these modes are active in the same parts of the domain as their associated low-frequency mode and have finer spatial structure. A primary difference is that these intermittent modes exhibit spatially propagating anomalies, as compared with their stationary SIC counterparts. This propagation is most evident in the subpolar gyre region of the North Atlantic.

4) SLP SPATIOTEMPORAL PATTERNS

Mode L_1^{SLP} (Fig. 7f) has a similar SLP pattern to the AO, with an anomaly centered over the pole and anomalies of opposite sign in the North Atlantic and North Pacific basins. The AO is defined as the leading

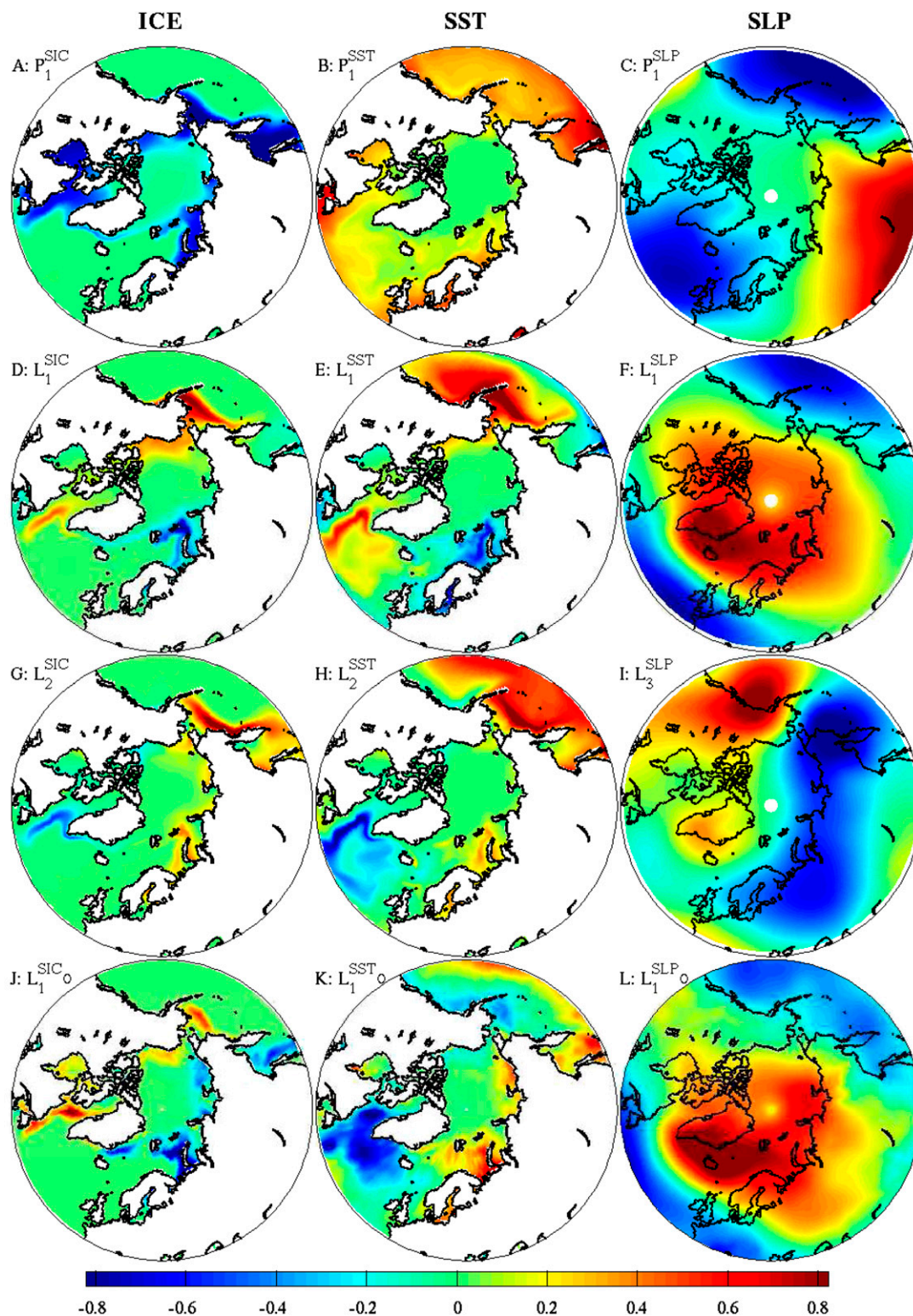


FIG. 7. Spatial patterns of selected sea ice, SST, and SLP NLSA modes. For each mode, we plot the spatial pattern with largest variance (of the q spatial patterns that make up the spatiotemporal pattern): (a)–(i) CCSM3 modes and (j)–(l) observational modes, indicated by an O subscript. The fields have been normalized to have a maximum absolute value of 1.

EOF of SLP north of 20°N. Considering EOFs of CCSM3 SLP north of 20°N, we find a maximum pattern correlation of 0.98 with EOF1. In light of this strong correlation, we call L_1^{SLP} the AO mode. Mode L_2^{SLP} also closely resembles the AO, with a maximum pattern correlation of 0.98 with EOF1. However, L_1^{SLP} and L_2^{SLP} have distinct temporal patterns and are nondegenerate modes.

Mode L_3^{SLP} (Fig. 7i) has a strong resemblance to the DA, which consists of opposite-signed SLP anomalies between the eastern and western Arctic. Following Wu et al. (2006), we define the dipole anomaly as the second leading EOF of winter (October–March) SLP north of 70°N. Let PC2 be the PC associated with EOF2. To determine the corresponding spatial pattern over the Arctic domain (north of 45°N), we project winter Arctic SLP onto PC2 and compare the resulting spatial pattern to L_3^{SLP} . We find a maximum pattern correlation of 0.78 and lower correlations when other PCs are used. Another possible technique for determining the Arctic SLP signal of the DA, as performed in Wu et al. (2006), is to perform a conditional composite, based on the months in which PC2 is active. This yields a very similar pattern correlation of 0.77 with L_3^{SLP} . Wu et al. (2006) also perform a conditional composite in which the influence of the AO is removed via linear regression. We also computed a spatial pattern using this technique and found a pattern correlation of 0.78 with L_3^{SLP} . Based on these findings, we refer to L_3^{SLP} as the DA mode.

Mode L_1^{SLP} has associated annual and semiannual intermittent modes $\{I_1^{\text{SLP}}, I_2^{\text{SLP}}, I_9^{\text{SLP}}, I_{10}^{\text{SLP}}\}$. Mode L_3^{SLP} is associated with a pair of annual intermittent modes $\{I_7^{\text{SLP}}, I_8^{\text{SLP}}\}$ but not any semiannual intermittent modes.

b. Observational modes

We compute the coupled NLSA observational modes using a locality parameter of $\epsilon = 1.20$ and a truncation level of $l = 21$ eigenfunctions. A primary difference between the observational modes and CCSM3 modes is the variables used for the eigenfunction computation. We find that computing SIC–SST–SLP eigenfunctions from the observational datasets yields temporal modes which are significantly noisier (more high-frequency power) than the corresponding modes from CCSM3. This corruption occurs because of the inclusion of the SLP data in the eigenfunction computation. We find that the eigenfunctions are substantially cleaner when computed using SIC and SST, and we use this as the base case for this study. On the other hand, the CCSM3 results are insensitive to the inclusion of SLP, with SIC–SST–SLP and SIC–SST eigenfunctions yielding very similar modes and conclusions regarding sea ice reemergence. We obtain SLP observational modes by

projecting the SLP data onto the SIC–SST eigenfunctions and performing an SVD of the resulting operator. Note that the observational SLP data is roughly 4 times finer spatial resolution than the CCSM3 SLP data. This discrepancy in resolution may explain the corruption in observational modes compared with CCSM3 modes. An NLSA kernel that incorporates an initial spatial smoothing of the input data (making them comparable to the T42 resolution of the CCSM3 data) could alleviate these issues, but we elected not to carry out these calculations since we are able to identify reemergence families ahead using SIC and SST only as inputs to the kernel.

The observational temporal modes have a similar character to those obtained from CCSM3. For each variable, we find periodic, low-frequency, and intermittent modes, and in many cases the low-frequency modes act as modulating envelopes for the intermittent modes. (The temporal modes for SIC, SST, and SLP are shown in the figures available as supplemental material at the Journals Online website: <http://dx.doi.org/10.1175/JCLI-D-14-00354.s2>.)

Next, we provide a brief description of the spatio-temporal modes that will be discussed later in the paper. Movies 3 and 4 in the online supplementary material provide a more revealing spatiotemporal evolution of these modes and others. Mode L_1^{SIC} (Fig. 7j) closely resembles the leading EOF of winter Arctic sea ice reported by Deser et al. (2000). In its positive phase, L_1^{SIC} has positive sea ice anomalies in the Labrador and Bering seas and negative anomalies in the Greenland Sea, Barents–Kara Seas, and Sea of Okhotsk. This mode has a maximum pattern correlation of 0.88 with EOF1 of Arctic sea ice from HadISST. Mode L_1^{SST} (Fig. 7k) is most similar to EOF2 of Arctic SST, with a maximum pattern correlation of 0.70. In positive phase, this mode has positive anomalies in the Labrador Sea and subpolar gyre region, negative anomalies in the Barents–Kara Seas and positive anomalies in the Bering Sea. Mode L_1^{SLP} (Fig. 7l) strongly resembles the annular structure of the AO. Computing EOFs of ERA-Interim SLP north of 20°N, we find a maximum pattern correlation of 0.97 with EOF1, the AO pattern. Similar to the CCSM3 results, the intermittent modes are generally associated with a low-frequency mode, are active in the same parts of the domain as this low-frequency mode, and display finer spatial structure.

One feature which is conspicuously absent from the observational SLP modes is a DA-like mode. Other fields, such as 850-hPa geopotential height and surface winds, and smaller domains were tested, but a low-frequency DA mode analogous to the CCSM3 results was not found. Certain modes obtained were quite transient and resembled the DA pattern at certain snapshots in time but not persistently.

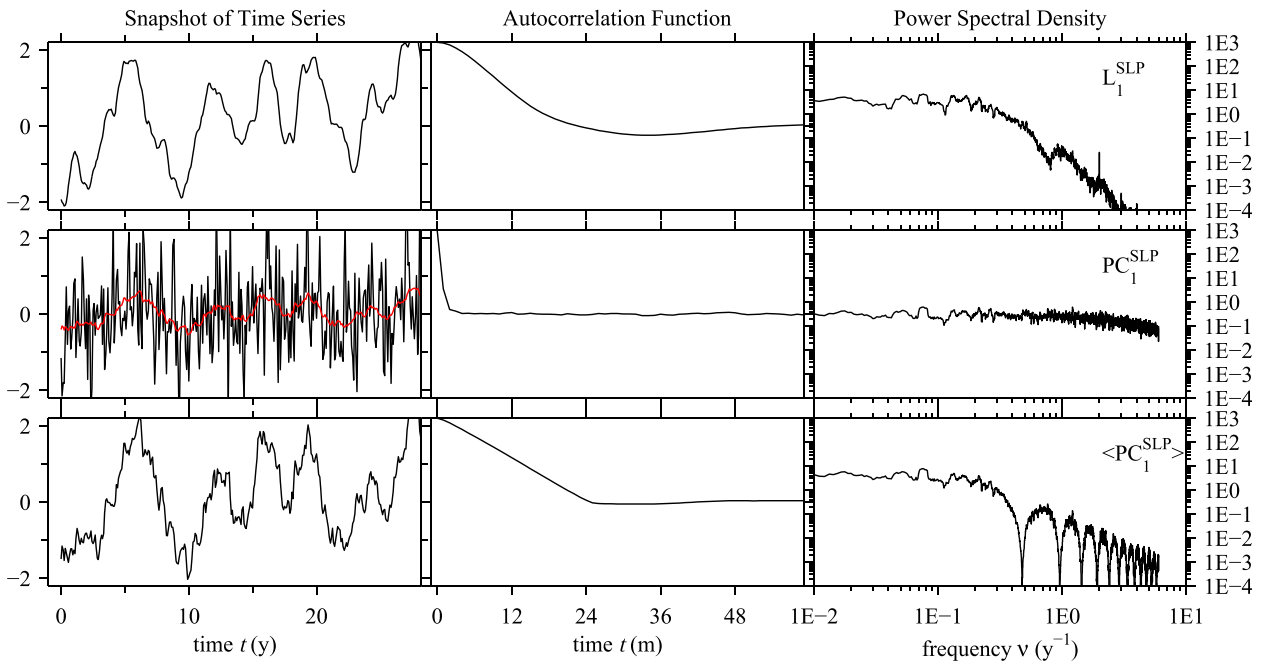


FIG. 8. Snapshots of the time series, power spectral density, and autocorrelation functions for (top) L_1^{SLP} , the leading low-frequency NLSA mode from CCSM3; (middle) PC_1^{SLP} , the principal component corresponding to the leading EOF of SLP; and (bottom) $\langle \text{PC}_1^{\text{SLP}} \rangle$, a low-pass-filtered version of PC_1^{SLP} , computed by taking a 24-month running mean. The red curve is $\langle \text{PC}_1^{\text{SLP}} \rangle$ plotted on top of PC_1^{SLP} . Note that the $\langle \text{PC}_1^{\text{SLP}} \rangle$ time series at bottom has been normalized to have a standard deviation of one.

c. Interpretation of low-frequency SLP modes

The low-frequency SLP modes have spatial patterns that closely resemble the familiar spatial patterns obtained via EOF analysis. However, their temporal behavior differs substantially. The low-frequency NLSA temporal modes have significant 1-yr autocorrelation and carry most of their power at frequencies below 1 yr^{-1} . This lies in sharp contrast to the PCs obtained via EOF analysis, which have a nearly white power spectrum and decorrelate very rapidly, losing all memory after 1–2 months. Despite these extremely different temporal characteristics, there is natural connection between the two: the low-frequency NLSA modes closely resemble a low-pass-filtered version of the noisy PCs from EOF analysis.

This is illustrated in Fig. 8, which shows temporal behavior for L_1^{SLP} , the leading low-frequency NLSA mode from CCSM3; PC_1^{SLP} , the principal component corresponding to the leading EOF of SLP; and $\langle \text{PC}_1^{\text{SLP}} \rangle$, a low-pass-filtered version of PC_1^{SLP} , computed by taking a 24-month running mean. Mode L_1^{SLP} has a relatively low correlation of 0.31 with PC_1^{SLP} but a significantly higher correlation of 0.80 with the low-pass-filtered PC $\langle \text{PC}_1^{\text{SLP}} \rangle$. Mode L_1^{SLP} and $\langle \text{PC}_1^{\text{SLP}} \rangle$ share qualitatively similar autocorrelation functions and power spectra, which are very different from the rapidly decaying

autocorrelation and nearly white power spectrum of PC_1^{SLP} . These results suggest a natural interpretation of the low-frequency NLSA modes as low-pass-filtered versions of the PCs from EOF analysis, which emphasize variability on interannual to decadal time scales and filter out higher-frequency variability. It is important to note that the low-frequency NLSA modes have weak sensitivity to the lag-embedding window Δt (as long as $\Delta t \geq 12$; see section 3). Also, a univariate NLSA analysis with only SLP was performed, and similar low-frequency modes were recovered. This suggests that these low-frequency patterns describe an intrinsic component of SLP variability, which in this case can be reproduced by an ad hoc running averaging of the data.

The observational SLP modes also display a similar correspondence, with a correlation of 0.83 between $\langle \text{PC}_1^{\text{SLP}} \rangle$ and L_1^{SLP} . This high correlation indicates that the SIC–SST eigenfunctions used for the observational data are able to capture important variability in the raw SLP data.

5. Arctic sea ice reemergence in models and observations

Sea ice reemergence is a time-lagged correlation phenomenon. SIC anomalies decorrelate over a 3–6-month time scale; however, at some time lag in the future, an

increase in correlation occurs. Sea ice reemergence is observed in two forms: a spring–fall reemergence, in which spring anomalies are reproduced the following fall, and a fall–spring reemergence, in which fall anomalies are reproduced the following spring. Both forms are observed in CCSM3 model output and HadISST observations, with the spring–fall reemergence being the significantly stronger signal in both cases.

We study sea ice reemergence via the time-lagged pattern correlation methodology of Bushuk et al. (2014). For each month of the year, pattern correlations are computed between the SIC anomaly field of the given month and the SIC field at lags of 0–23 months into the future. This is done for all pairs (month, month + lag) in the time series, and we report the average of these correlation values. Note that the pattern correlations are performed on anomalies from the seasonal cycle, are area weighted, and are uncentered (global mean has not been subtracted from the anomaly field). This differs from the approach of Blanchard-Wrigglesworth et al. (2011), where the lagged correlations were performed using a time series of total sea ice area. Performing correlations using the full SIC field, as opposed to its total area, allows for inclusion of the spatial distribution of sea ice. The pattern correlation approach is able to detect opposite-signed anomaly features, such as sea ice dipoles, which would be integrated away in the total area approach. It also enforces a notion of locality, since anomalies must be spatially coincident in order to yield a significant pattern correlation. This ensures that a reported sea ice reemergence signal represents recurrent anomalies at the same spatial location.

In this paper, we focus on the regions defined in Fig. 1: a pan-Arctic domain (45°–90°N over all longitudes), the Barents and Kara Seas (65°–80°N, 30°–90°E), the Labrador Sea and Baffin Bay (45°–80°N, 70°–40°W), the Greenland Sea (55°–80°N, 40°W–0°), the Bering Sea (55°–65°N, 165°E–160°W), and the Sea of Okhotsk (45°–65°N, 135°–165°E).

a. Regional sea ice reemergence in models and observations

We begin with a regional study of sea ice reemergence using raw SIC data from HadISST observations and CCSM3 output: the results of which are shown in Fig. 9. This figure shows time-lagged pattern correlations, computed for all initial months and lags of 0–23 months. All correlations plotted in color are greater than 0.1 and are significant at the 95% level, based on a *t*-distribution statistic, which tests for the statistical significance of the time-mean pattern correlation values against a null hypothesis that there is no correlation.

Over a pan-Arctic domain, in both the model and observations, we observe a clear “summer limb” of

positive correlations corresponding to sea ice anomalies that originate in the melt season (March–August) and reemerge in the growth season (Figs. 9a,b). The “winter limb” of fall–spring reemergence, corresponding to anomalies originating in September–February, is weak over the Arctic domain, except for a small hint of the limb in the CCSM3 data. An interesting consequence of the time-lagged pattern correlation approach is the striking similarity of pan-Arctic lagged correlations in CCSM3 and observations. This lies in contrast to the total area lagged correlation methodology of previous studies, which reveal a clearly enhanced reemergence signal in the model relative to observations (Blanchard-Wrigglesworth et al. 2011; Day et al. 2014). This indicates that, despite differences in memory of total sea ice area anomalies, the model and observations are quite similar in their memory of sea ice spatial patterns.

The pan-Arctic reemergence signal is similar in the model and observations; however, a regional analysis reveals significant differences between the two. Both CCSM3 and HadISST have strong summer limb signals in the Barents–Kara Seas (Figs. 9g,h) and the Greenland Sea (Figs. 9k,l). The CCSM3 data also exhibit a winter limb in the Barents–Kara Seas, which is not significant in observations. A striking difference is found in the Labrador Sea, with a strong summer limb and a significant winter limb in observations: neither of which is found in the model (Figs. 9i,j). Conversely, the strong summer limbs in the Bering Sea and Sea of Okhotsk found in the model data are absent in the observations (Figs. 9c–f). Note that the winter limb signal in the Bering Sea and Sea of Okhotsk should not be overinterpreted, as these domains are essentially sea ice free during the summer and early fall. Therefore, the North Pacific winter limb lagged correlations are performed using an extremely low-variance signal and are not robust.

b. Sea ice reemergence revealed via coupled NLSA

Given the nontrivial lagged correlation structures in the CCSM3 and HadISST sea ice datasets, we seek a low-dimensional representation of sea ice reemergence via the coupled NLSA modes obtained in section 4. We aim to answer two main questions: 1) Can the reemergence signal of the raw data be efficiently reproduced by low-dimensional families of modes? 2) Can these mode families reveal possible mechanisms for Arctic sea ice reemergence? To answer the former, we perform time-lagged pattern correlations using small subsets of reconstructed spatiotemporal fields from coupled NLSA. Our approach here is to first construct families of SIC modes and then to augment these families with SST and SLP modes, based on correlations.

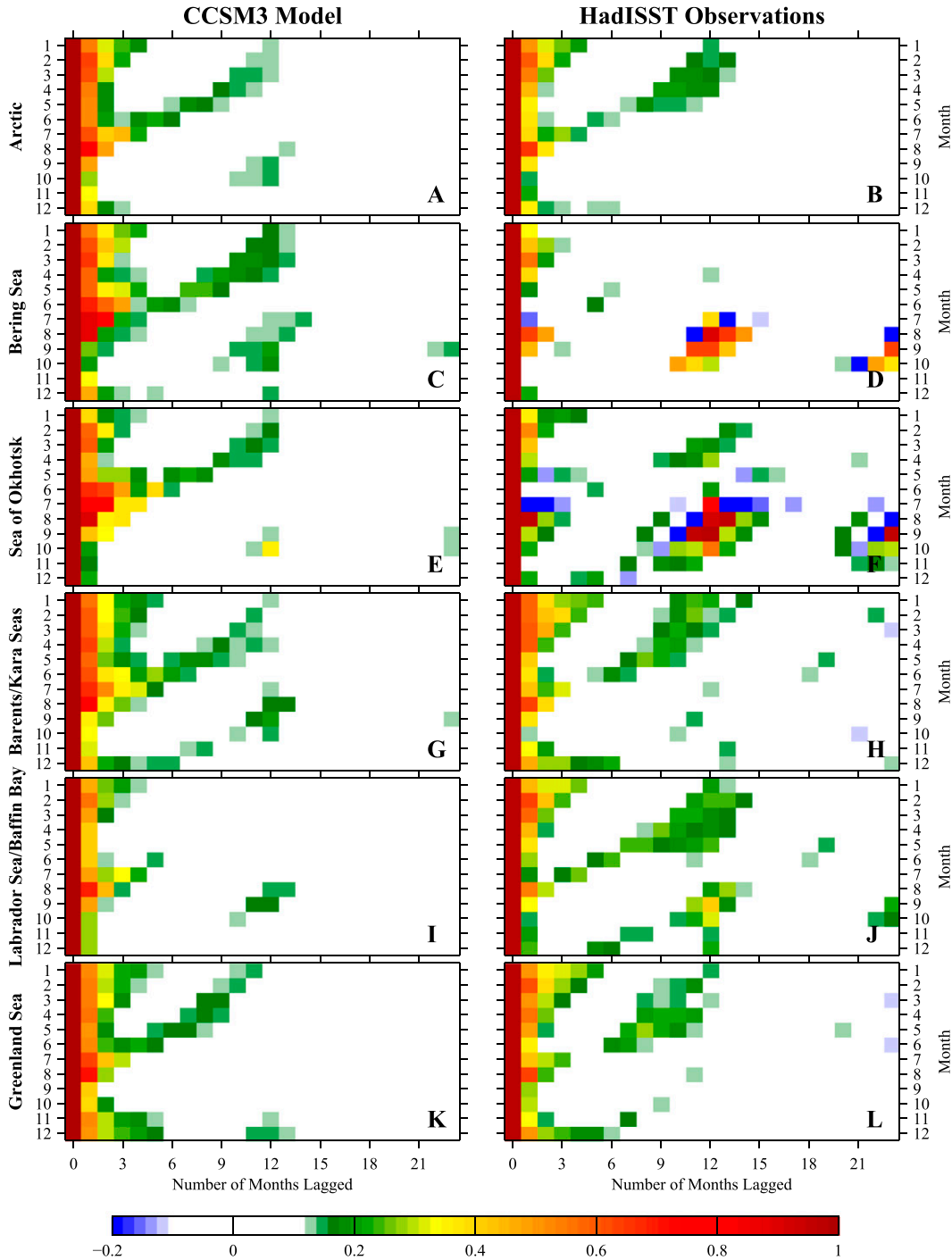


FIG. 9. Time-lagged pattern correlations of Arctic sea ice in different regions: (left) results from CCSM3 model output and (right) results from HadISST observations. All colored boxes are significant at the 95% level, based on a t test.

1) CCSM3 REEMERGENCE FAMILIES

Based on the associations between low-frequency and intermittent modes identified in section 4a(1), we construct two families of SIC modes, each consisting

of a low-frequency mode and annual and semi-annual intermittent modes. These families, which we refer to as \mathcal{F}_1^M and \mathcal{F}_2^M , are able to qualitatively reproduce the reemergence signal of the raw data. They are given by $\mathcal{F}_1^M = \{L_1^{SIC}, I_1^{SIC}, I_2^{SIC}, I_7^{SIC}, I_8^{SIC}\}$ and

$\mathcal{F}_2^M = \{L_2^{\text{SIC}}, I_3^{\text{SIC}}, I_4^{\text{SIC}}, I_9^{\text{SIC}}, I_{10}^{\text{SIC}}, I_{11}^{\text{SIC}}\}$. Here, the M superscript indicates that these families come from model output. Each family is particularly active in the Barents–Kara, Bering, and Labrador Seas but shares different phase relationships between the different regions. Within each family, the low-frequency and intermittent modes are closely related, in the sense that the low-frequency mode provides the modulating envelope for the intermittent modes. This means that all modes in a given family tend to be active or inactive at the same times. Note that similar envelope associations were observed in the reemergence families identified in Bushuk et al. (2014), suggesting that this approach may be useful in a broader context. Many other mode subsets were tested but were unable to reproduce the lagged correlation structure as effectively as these families, likely because they lack the envelope relationships that characterize the families. Moreover, \mathcal{F}_1^M and \mathcal{F}_2^M appear to be the minimal mode subsets, as smaller sets are unable to qualitatively reproduce the reemergence signal.

In Fig. 10d, we show time-lagged pattern correlations computed over the Arctic domain using NLSA family \mathcal{F}_1^M . Comparing with the time-lagged pattern correlation structure of the raw data, shown in Fig. 10a, we observe qualitatively similar features. The \mathcal{F}_1^M correlations have a clear summer limb structure, with correlations that decay to near zero over the summer months and reemerge the following fall. They also have a slightly weaker winter limb, which may correspond to the weaker fall–spring reemergence seen in the raw data. The \mathcal{F}_1^M correlations are substantially higher than the raw data correlations because the family’s activity is primarily governed by L_1^{SIC} , which has a decorrelation time of 3 years.

This NLSA family has a qualitatively similar correlation structure to the raw data, yet it is natural to ask whether this family is capturing the portion of the signal responsible for the summer limb in the raw data. As a method for addressing this question, we compute time-lagged cross correlations between the raw data and the NLSA subspaces, shown in Figs. 10b,c. To explain Figs. 10b,c, we introduce $\text{LC}(A, B)$, a function that computes time-lagged pattern correlations, with the dataset B lagging A . Using this notation, Fig. 10a shows $\text{LC}(\text{Raw}, \text{Raw})$ and Fig. 10d shows $\text{LC}(\mathcal{F}_1^M, \mathcal{F}_1^M)$. In Figs. 10b and 10c, we plot $\text{LC}(\text{Raw}, \mathcal{F}_1^M)$ and $\text{LC}(\mathcal{F}_1^M, \text{Raw})$, respectively.

If the reemergence signal of \mathcal{F}_1^M is not representative of the signal in the raw data, one would expect these cross correlations to be small. However, we observe strong summer limbs in Figs. 10b,c, similar to the correlation structure of the raw data. The fact that these panels are similar to Fig. 10a indicates that family \mathcal{F}_1^M is

capturing the portion of the data responsible for the sea ice reemergence signal.

In Figs. 10e–h, we plot the same quantities as Figs. 10a–d but for family \mathcal{F}_2^M . The lagged correlations $\text{LC}(\mathcal{F}_2^M, \mathcal{F}_2^M)$ also have a strong summer limb and a weaker winter limb, but each of these limbs is weaker than their respective counterparts in $\text{LC}(\mathcal{F}_1^M, \mathcal{F}_1^M)$. Also, $\text{LC}(\text{Raw}, \mathcal{F}_2^M)$ and $\text{LC}(\mathcal{F}_2^M, \text{Raw})$, plotted in Figs. 10f and 10g, show partial summer limbs, but these correlations are weaker than the reemergence signal of the raw data. This indicates that family \mathcal{F}_2^M is capturing some of the reemergence signal but not as significant a portion as family \mathcal{F}_1^M .

2) HADISST REEMERGENCE FAMILIES

The observational modes also admit a mode family that is able to reproduce the reemergence signal of the raw HadISST. This family is given by $\mathcal{F}_1^O = \{L_1^{\text{SIC}}, I_1^{\text{SIC}}, I_2^{\text{SIC}}, I_5^{\text{SIC}}, I_6^{\text{SIC}}\}$, where the O indicates observational data. There is no clear second family that has nontrivial cross correlations with the raw observational data. In Fig. 11 we plot time-lagged cross correlations for \mathcal{F}_1^O . The lagged correlations $\text{LC}(\mathcal{F}_1^O, \mathcal{F}_1^O)$ have a clear summer limb and a weaker winter limb. We also find a strong summer limb structure in $\text{LC}(\text{Raw}, \mathcal{F}_1^O)$ and $\text{LC}(\mathcal{F}_1^O, \text{Raw})$, except for a small gap in the limb for anomalies beginning in July. This indicates that the family \mathcal{F}_1^O is capturing a substantial portion of the reemergence signal in the raw data.

c. Variance explained by reemergence families

Another way to test the effectiveness of the families in capturing the reemergence signal is to directly subtract the families from the raw sea ice data and compute time-lagged pattern correlations on the resulting dataset. Figure 12c shows $\text{LC}(\text{Raw} - \mathcal{F}_1^M - \mathcal{F}_2^M, \text{Raw} - \mathcal{F}_1^M - \mathcal{F}_2^M)$, and Fig. 12d shows $\text{LC}(\text{Raw} - \mathcal{F}_1^O, \text{Raw} - \mathcal{F}_1^O)$. Each of these has a clearly reduced summer limb relative to $\text{LC}(\text{Raw}, \text{Raw})$, which are shown in Fig. 12a for CCSM3 and Fig. 12b for HadISST. This demonstrates that the reemergence families are capturing a substantial portion of the reemergence signal. In terms of total sea ice area anomalies, family \mathcal{F}_1^M explains 41%, 25%, and 8% of the variance in the Bering, Barents–Kara, and Labrador Seas, respectively. Similarly, \mathcal{F}_2^M explains 18%, 1%, and 14% of the variance, and \mathcal{F}_1^O explains 7%, 30%, and 18% of the variance in these respective regions.

The variance explained by these families is lower if one considers the full (nonintegrated) sea ice anomaly field. Over the full Arctic domain family \mathcal{F}_1^M explains 5% of the variance, \mathcal{F}_2^M explains 3%, and \mathcal{F}_1^O explains 7%. While these values seem somewhat low, it is interesting to note that the leading two EOFs from CCSM3 capture 7% and

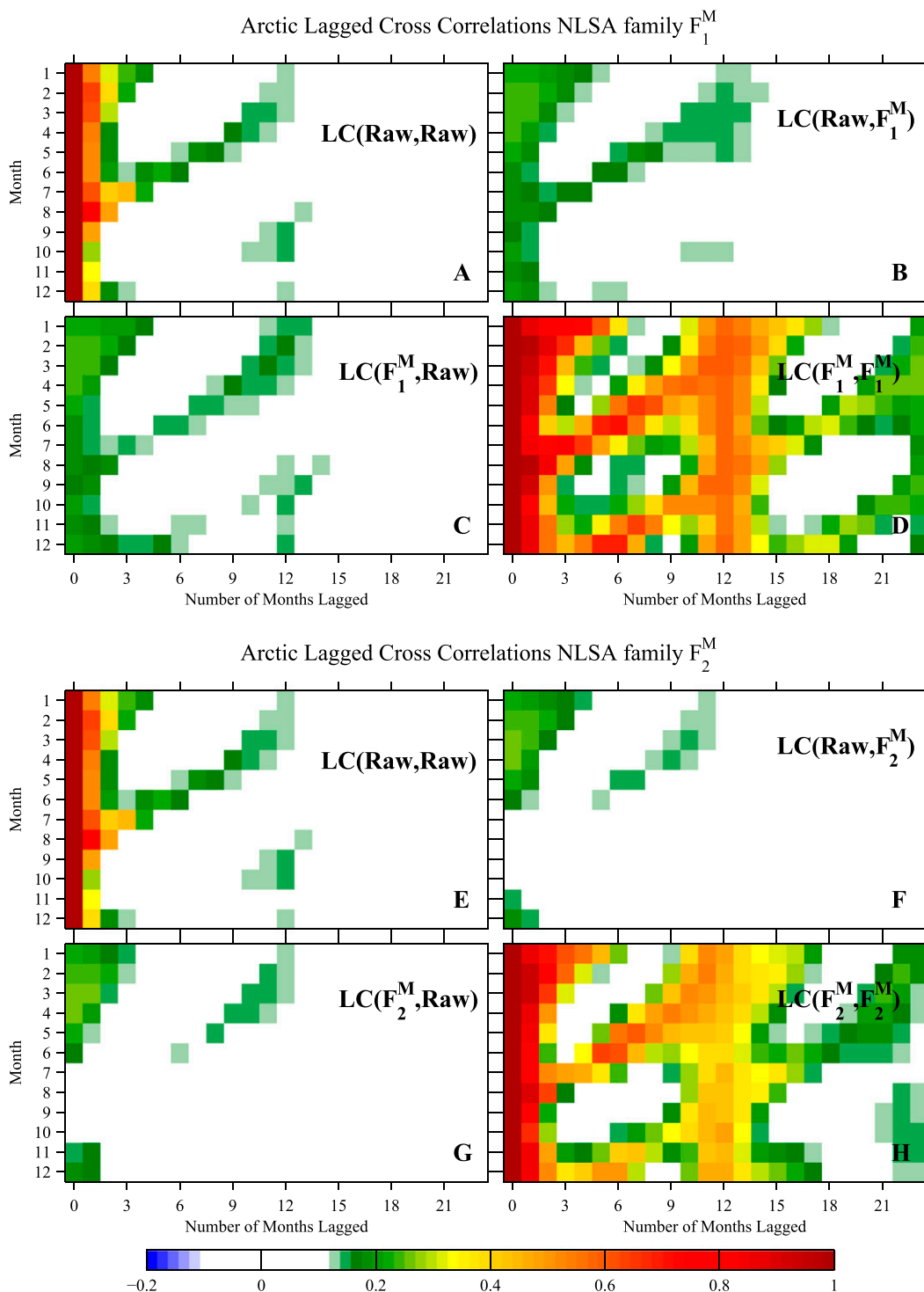


FIG. 10. Time-lagged pattern correlations of sea ice computed over the Arctic domain, using NLSA families \mathcal{F}_1^M and \mathcal{F}_2^M : shown are correlations of (a) the raw data and (d) \mathcal{F}_1^M and cross correlations of \mathcal{F}_1^M and the raw data, with the NLSA data (b) lagging and (c) leading. (e)–(h) As in (a)–(d), but for \mathcal{F}_2^M . All colored boxes are significant at the 95% level.

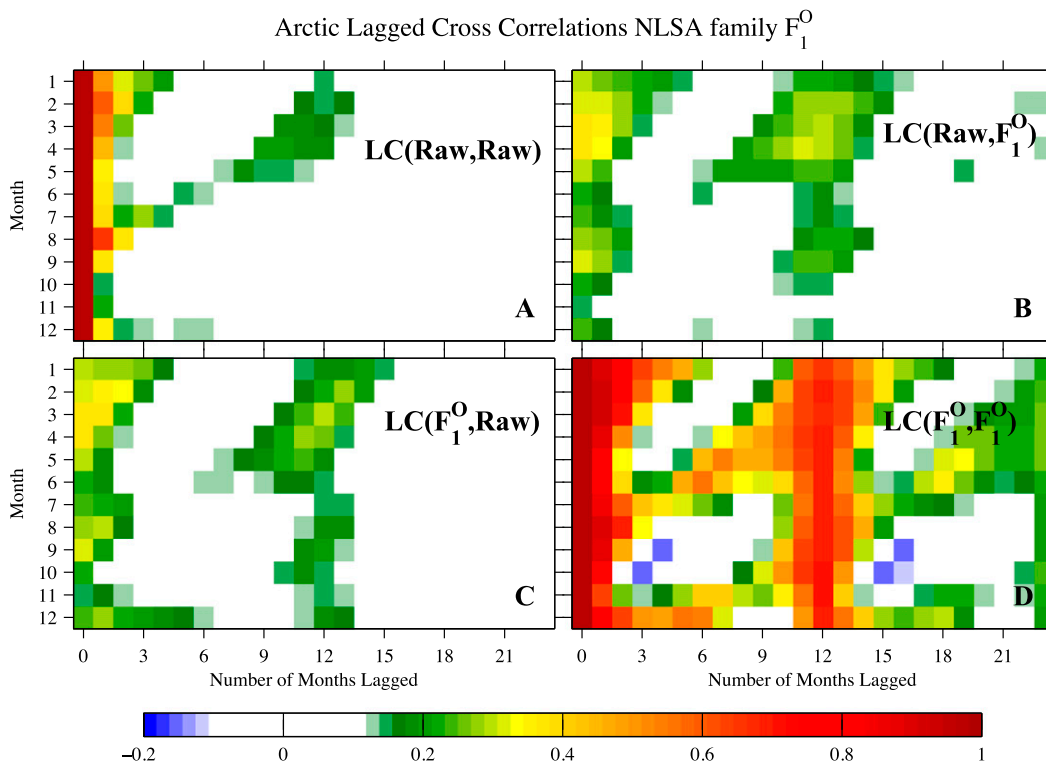


FIG. 11. Time-lagged pattern correlations of sea ice computed over the Arctic domain, using HadISST family \mathcal{F}_1^O : shown are correlations of (a) the raw data and (d) NLSA family \mathcal{F}_1^O and cross correlations of \mathcal{F}_1^O and the raw data, with the NLSA data (b) lagging and (c) leading. All colored boxes are significant at the 95% level.

6% of the variance, respectively. These values are lower than those typically reported in EOF studies for three reasons: 1) the spatial domain is large; 2) there has been no temporal smoothing or averaging performed; and 3) the spatial resolution is relatively fine. For example, the leading EOF of Deser et al. (2000) captures 35% of the sea ice variance in the Arctic, but this is based on a time series of winter-mean sea ice anomalies. This temporal averaging substantially smooths the data, and the leading EOF captures variance more efficiently in this time-filtered dataset. By contrast, the leading 10 EOFs of CCSM3 Arctic sea ice capture 38% of the variance.

The comparison with SSA, a variance greedy algorithm, is also illuminating. The leading two SSA modes capture 2.5% and 2% of the variance, respectively, and the leading 10 nonperiodic SSA modes capture 14% of the variance. By comparison, the leading 10 nonperiodic NLSA modes capture 10% of the variance, which is modestly less than SSA. The main reason for this discrepancy is that the intermittent modes of NLSA carry less variance than low-frequency modes. Despite being low variance, these intermittent modes are crucial components of the reemergence families and illustrate an important point: low-variance modes can play an important role in explaining dynamical phenomena.

d. Temporal variability of sea ice reemergence

To this point, all reported lagged correlations have been time-mean values, computed over the full time series. Next, we consider the time-dependent aspects of sea ice reemergence. Figure 12e shows lagged correlations of the raw CCSM3 sea ice data, conditional on the low-frequency modes of \mathcal{F}_1^M or \mathcal{F}_2^M (L_1^{SIC} and L_2^{SIC}) being active. Specifically, we condition on all times for which $|L_1^{\text{SIC}}(t)| > 2$ or $|L_2^{\text{SIC}}(t)| > 2$ (which corresponds to 11% of the data). Similarly, Fig. 12f shows lagged correlations of the raw HadISST conditional on the low-frequency mode of \mathcal{F}_1^O being active [$|L_1^{\text{SIC}}(t)| > 1.5$, which corresponds to 14% of the data]. We observe a clearly enhanced reemergence signal (both summer and winter limbs) during times when these modes are active. Figures 12g and 12h show lagged correlations conditional on these modes being inactive [$|L_1^{\text{SIC}}(t)| < 1$ and $|L_2^{\text{SIC}}(t)| < 1$ for CCSM3 and $|L_1^{\text{SIC}}(t)| < 1$ for HadISST]. This corresponds to 45% and 59% of the data, respectively. In both cases, particularly with CCSM3, we observe a diminished reemergence signal. These results indicate that reemergence events have significant temporal variability, characterized by regimes of quiescence and other regimes of intense activity. Another notable

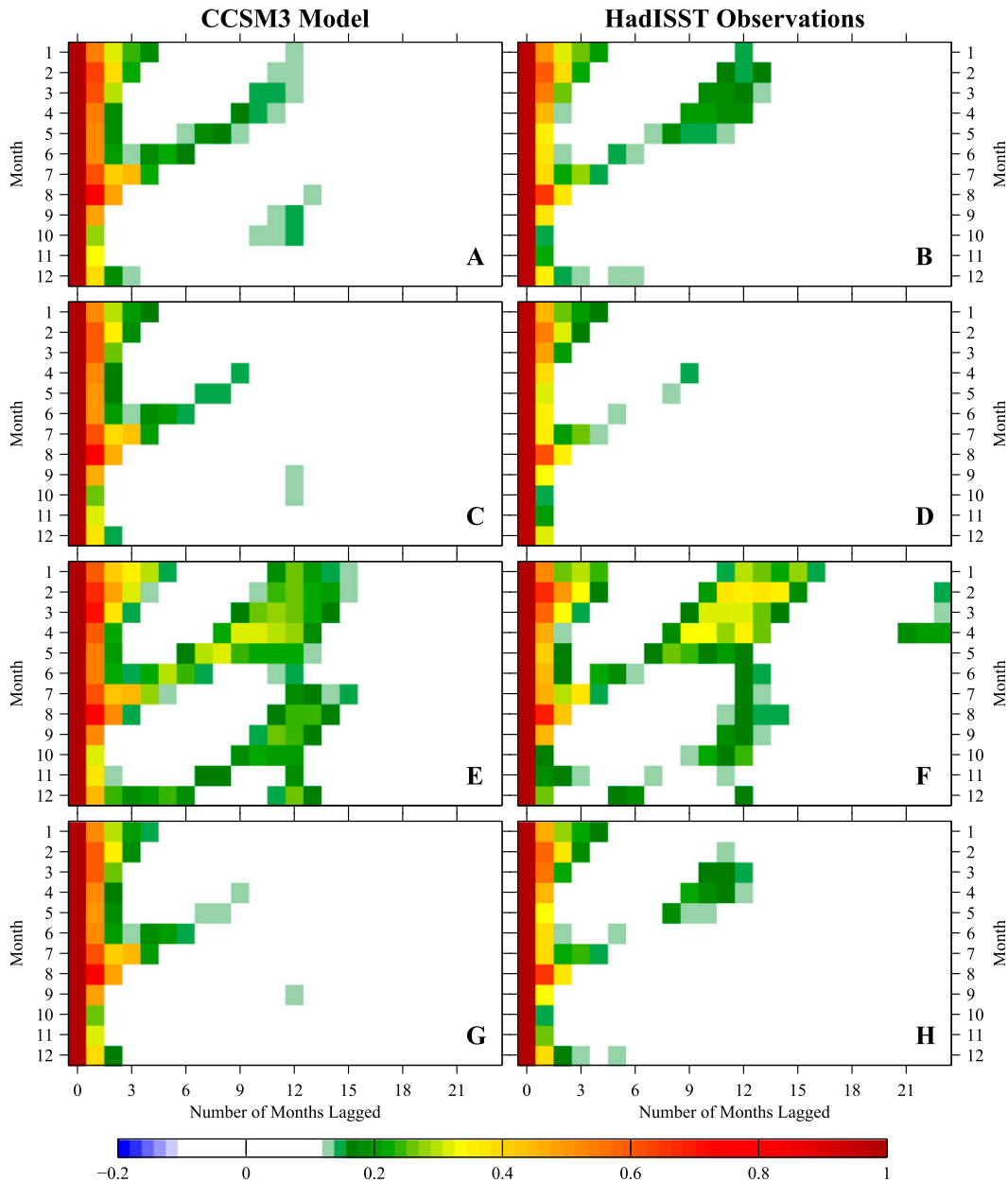


FIG. 12. Time-lagged pattern correlations of sea ice computed over the Arctic domain. Lagged correlations for CCSM3 data are shown for (a) the raw data, (c) $\text{Raw} - \mathcal{F}_1^M - \mathcal{F}_2^M$, (e) conditional on $|L_1^{\text{SIC}}(t)| > 2$ or $|L_2^{\text{SIC}}(t)| > 2$ (which corresponds to 11% of the data), and (g) conditional on $|L_1^{\text{SIC}}(t)| < 1$ and $|L_2^{\text{SIC}}(t)| < 1$ (45% of the data). HadISST lagged correlations are shown for (b) the raw data, (d) $\text{Raw} - \mathcal{F}_1^O$, (f) conditional on $|L_1^{\text{SIC}}(t)| > 1.5$ (which corresponds to 14% of the data), and (h) conditional on $|L_1^{\text{SIC}}(t)| < 1$ (59% of the data).

feature is the robust initial decay of correlation for lags of 0–3 months. The most significant differences between Figs. 12e,f and Figs. 12g,h occur at lags greater than 3 months, indicating that reemergence events display more temporal variability than the initial decay of persistence. Note that, because of the shortness of observational record, the conditional correlations from HadISST are less robust than those from CCSM3.

In CCSM3, about half of the record is characterized by a very weak reemergence signal (Fig. 12g), whereas other times exhibit strong reemergence (Fig. 12e). This may have important implications for sea ice predictability, since predictability resulting from reemergence will have a strong temporal dependence, dependent on the strength of the reemergence signal at a given time. The results here also demonstrate the efficacy of certain low-frequency

NLSA modes as predictors for the strength of reemergence events. Therefore, these modes could be a valuable addition to statistical sea ice forecast models.

As another method to test the temporal variability of reemergence events, we measure the strength of the reemergence signal as a function of time. We define the reemergence strength as the sum of correlation values along the summer limb, compute this quantity for each year of the time series, and create a probability density function (PDF). The PDF (not shown) is close to Gaussian, with a slight skew toward large reemergence events. If we let μ be the mean of the PDF, we find that 23% of reemergence events are less than 0.5μ and 23% of events are greater than 1.5μ . This spread in event distribution demonstrates that reemergence strength fluctuates strongly in time.

This temporal characterization of Arctic reemergence events is a new result of this study, which was inaccessible in previous studies of reemergence based on time-lagged total area correlations. In the time-lagged pattern correlation methodology, correlations are performed space, rather than time, which allows for the temporal variations of these correlations to be studied. The mode families also allow for an investigation of the temporal variability of reemergence events and mechanisms, and this will be returned to later in section 6c.

e. SIC–SST–SLP reemergence families

We have identified families of coupled NLSA SIC modes that are able to reproduce the reemergence signal of the raw SIC data. Next, we focus on the spatiotemporal evolution of these families and their associated SST and SLP patterns. As noted earlier, there are strong correlations between the temporal modes of SIC, SST, and SLP. We use this fact to augment the families \mathcal{F}_1^M , \mathcal{F}_2^M , and \mathcal{F}_1^O with associated SST and SLP modes.

The low-frequency mode of \mathcal{F}_1^M is L_1^{SIC} . Performing correlations between this mode and all low-frequency SST and SLP PCs, we find maximum correlations of -0.99 with L_1^{SST} and -0.69 with L_3^{SLP} . Similarly, for the L_2^{SIC} mode of \mathcal{F}_2^M , we find maximum correlations of -0.93 with L_2^{SST} and 0.64 with L_1^{SLP} . For the observational family \mathcal{F}_1^O , we find that L_1^{SIC} has maximum correlations of 0.998 with L_1^{SST} and -0.81 with L_1^{SLP} . Note that the low-frequency mode correlations are higher between SIC and SST than between SIC and SLP, indicating that the temporal covariability between SIC and SST is somewhat stronger.

Each family consists of a low-frequency mode and associated annual and semiannual intermittent modes. To form the augmented families, we identify the intermittent modes associated with the low-frequency SST and SLP modes identified above. Based on the envelope

correlations shown in Fig. 6, we define the following augmented families:

$$\mathcal{F}_1^M = \{L_1^{\text{SIC}}, I_{\{1,2,7,8\}}^{\text{SIC}}, L_1^{\text{SST}}, I_{\{2,3,8,9\}}^{\text{SST}}, L_3^{\text{SLP}}, I_{\{7,8\}}^{\text{SLP}}\},$$

$$\mathcal{F}_2^M = \{L_2^{\text{SIC}}, I_{\{3,4,9,10,11\}}^{\text{SIC}}, L_2^{\text{SST}}, I_{\{5,6,11\}}^{\text{SST}}, L_1^{\text{SLP}}, I_{\{1,2,9,10\}}^{\text{SLP}}\},$$

and

$$\mathcal{F}_1^O = \{L_1^{\text{SIC}}, I_{\{1,2,5,6\}}^{\text{SIC}}, L_1^{\text{SST}}, I_{\{1,2,7,8\}}^{\text{SST}}, L_1^{\text{SLP}}, I_{\{1\}}^{\text{SLP}}\}.$$

Here, the intermittent mode indices are given in braces for each variable.

6. Sea ice reemergence mechanisms

a. SST–sea ice reemergence mechanism

We now examine the sea ice reemergence mechanisms suggested by the SIC–SST–SLP families defined above. Bushuk et al. (2014) showed that low-dimensional families of NLSA modes produce an SST–sea ice reemergence mechanism in the North Pacific sector, which is consistent with that proposed by Blanchard-Wrigglesworth et al. (2011). Can a similar mechanism be observed in Arctic NLSA modes? In both the model and observations, the answer is yes.

Figure 13 shows spatial reconstructions of SIC, SST, and SLP using family \mathcal{F}_1^M . These spatial patterns are composites, produced by averaging over all times where $L_1^{\text{SIC}}(t) > 1$ (which corresponds to 17% of the data). Similar patterns, with opposite sign, are obtained by compositing over times when $L_1^{\text{SIC}}(t)$ is in negative phase. This figure shows four months of the year, but the time evolution of \mathcal{F}_1^M , shown in movie 5 in the online supplementary material, is much more illuminating.

In the winter months of January–March, we observe strong negative sea ice anomalies in the Barents Sea and strong positive anomalies in the Bering and Labrador Seas. These anomalies reach their maximum southerly extent in March. We observe SST anomalies of opposite sign, which are roughly spatially coincident with the sea ice anomalies but also extend farther south in each of the three seas. Note that in March the Kara Sea, the northern Bering Sea, and the northern Labrador Sea are all SST anomaly free. The ice anomalies move northward and weaken over the melt season, which begins in April. In June, the ice anomalies in the region of the Barents–Kara Seas are located primarily in the Kara Sea. Also, the Bering and Labrador anomalies have moved into the northern parts of these seas and weakened substantially.

As the ice anomalies move northward, they imprint an anomaly of opposite sign in the SST field. In particular,

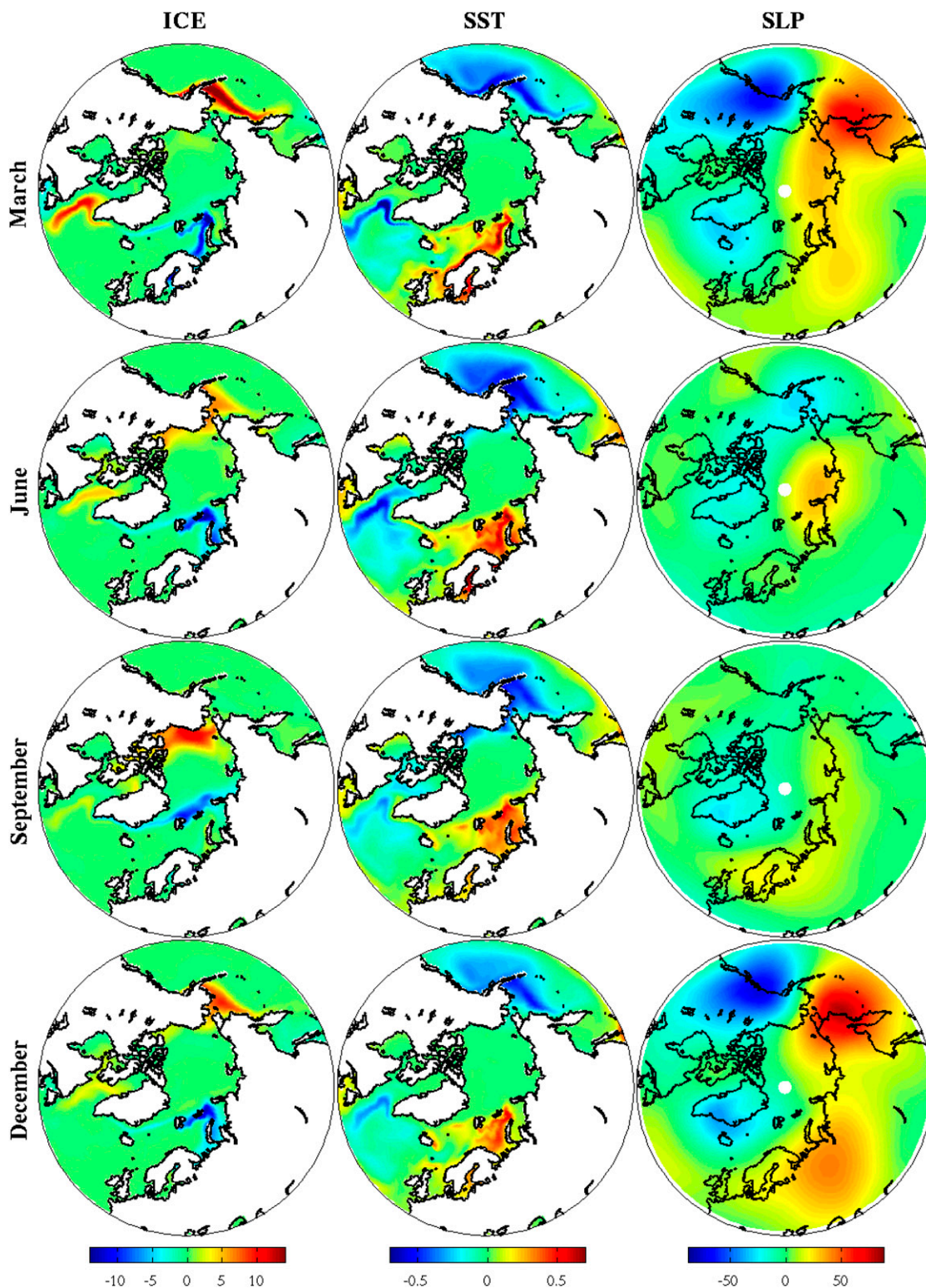


FIG. 13. Sea ice, SST, and SLP patterns of CCSM3 reemergence family \mathcal{F}_1^M at different months of the year. These spatial patterns are composites, obtained by averaging over all years in which $L_1^{\text{SIC}} > 1$.

the previously anomaly-free Kara and northern Bering and Labrador Seas now have strong SST anomalies. The ice continues to retreat northward over the melt season, reaching its minimum extent in September. In September, the sea ice anomalies are extremely weak in the Barents–Kara, Bering, and Labrador Seas, yet each of these seas has retained an SST anomaly. The SST anomaly retained in the Barents–Kara and Bering Seas is particularly strong, with a weaker anomaly in the Labrador Sea. As the growth season begins, the ice moves southward, interacts with the SST anomalies that have been stored over the summer months, and re-inherits anomalies of the same sign as the previous spring. In December, we observe that most of the summer imprinted SST anomalies have disappeared, and the sea ice anomalies have reemerged with the same sign as the spring anomalies. This reemergence family is typically active for a 2–8-yr period, during which we observe re-emerging sea ice anomalies of a consistent sign (see movie 5 in the online supplementary material).

We observe a similar SST–sea ice reemergence mechanism in family \mathcal{F}_2^M , shown in Fig. 14 and movie 6 in the online supplementary material. This figure is based on a composite over all times in which $L_2^{\text{SIC}} > 1$ (which corresponds to 16% of the data). This family exhibits strong winter sea ice anomalies in the Bering and Labrador Seas, which are out of phase with each other. These anomalies disappear over the melt season, leaving an SST imprint in the northern parts of these seas in June and September. We observe a sea ice reemergence during the growth season, as the SST anomalies are converted into ice anomalies. This family does not have a strong signal in the Barents–Kara Seas.

The observational family \mathcal{F}_1^O displays a clear sea ice reemergence, which is active primarily in the Sea of Okhotsk and the Barents–Kara, Bering, Labrador, and Greenland Seas (movie 7 in the online supplementary material). This family, shown for the year 1991 in Fig. 15, also displays the SST–sea ice reemergence mechanism, but in a slightly less clean manner than the model output. The \mathcal{F}_1^O has positive winter sea ice anomalies in the Bering and Labrador Seas, and negative anomalies in the Barents–Kara Seas, Greenland Sea, and Sea of Okhotsk. The family has winter SST anomalies of opposite sign to these sea ice anomalies, which extend southward of the sea ice anomalies. Comparing the March panels to the June and September panels, an SST imprinting can be observed in the Barents–Kara Seas and, to a lesser extent, the Labrador and Bering Seas. Sea ice anomalies of the same sign reappear in the fall, and this pattern roughly repeats the following year.

The reemergence families are able to capture the SST–sea ice mechanism of Blanchard-Wrigglesworth

et al. (2011), previously only accessible via time correlation analysis of raw sea ice and SST fields. This mode-based representation of reemergence allows one to track the temporal variability and strength of the SST–sea ice reemergence mechanism, as will be done later in section 6c. Also, the low dimensionality of these families has implications for predictability, since a small number of predictors (specifically the low-frequency modes of the families) define the amplitude and sign of reemergence events.

b. Sea ice teleconnections and reemergence via low-frequency SLP variability

Movies 5–7 in the online supplementary material reveal consistent phase relationships between sea ice anomalies in the Barents–Kara, Bering, and Labrador Seas. The SST mechanism described above provides a local mechanism for sea ice reemergence but does not explain this phase locking between geographically disconnected seas. We find that the SLP patterns of \mathcal{F}_1^M , \mathcal{F}_2^M , and \mathcal{F}_1^O (shown in the right panels of Figs. 13–15) provide pan-Arctic-scale teleconnections between these different regions.

We begin with family \mathcal{F}_1^M (Fig. 13), which has an SLP pattern closely resembling the DA. This pattern is characterized by four main centers of action: pressure anomalies of the same sign over Greenland and northwest North America and opposite-signed anomalies over western Russia and eastern Siberia. The geostrophic winds associated with this SLP pattern are primarily meridional, blowing across the Arctic from the Bering Sea to the Barents–Kara Seas, or vice versa. We find that the ice advection and surface air temperature advection associated with these large-scale winds is consistent with the observed phase relationships in regional sea ice anomalies.

From January to March, the dipole anomaly is very active, with strong northerly winds over the Bering Sea and strong southerly winds over the Barents–Kara Seas. The northerly winds advect cold Arctic air over the Bering Sea and also push the ice edge southward and advect additional ice into the sea. Each of these effects encourages the formation of a positive sea ice anomaly in the Bering Sea. Similarly, the Barents–Kara Seas experience warm southerly winds, which melt additional ice and also push the ice edge northward, contributing to the observed negative sea ice anomaly. Also, the SLP anomaly centered over Greenland produces northerly geostrophic winds over the Labrador Sea, contributing to its positive sea ice anomalies for the same reasons. The SLP anomalies and corresponding winds weaken substantially over the summer months, as do the sea ice anomalies in each of these regions. In October, the SLP

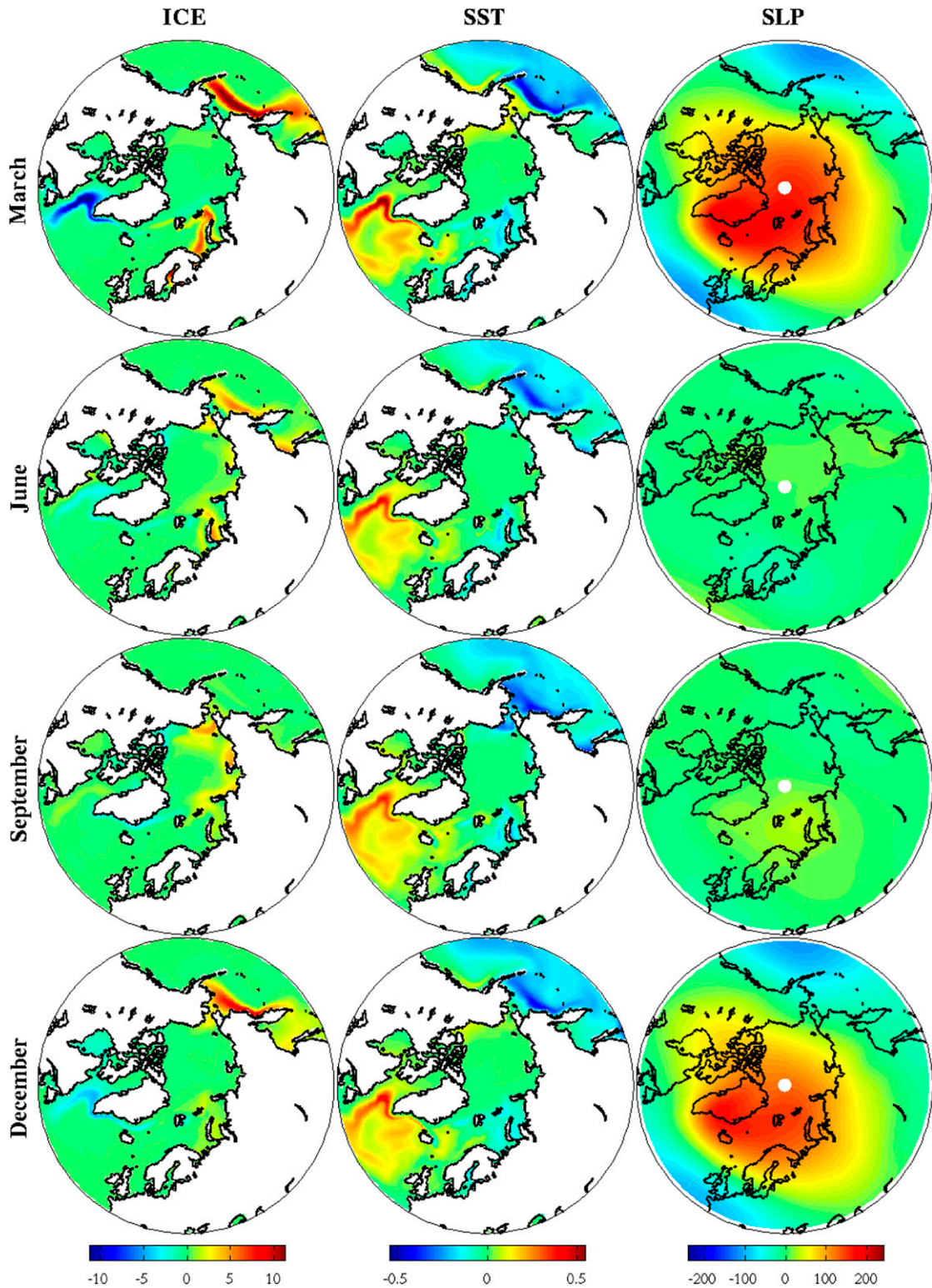


FIG. 14. Sea ice, SST, and SLP patterns of CCSM3 reemergence family \mathcal{F}_2^M at different months of the year. These spatial patterns are composites, obtained by averaging over all years in which $L_2^{\text{SIC}} > 1$.

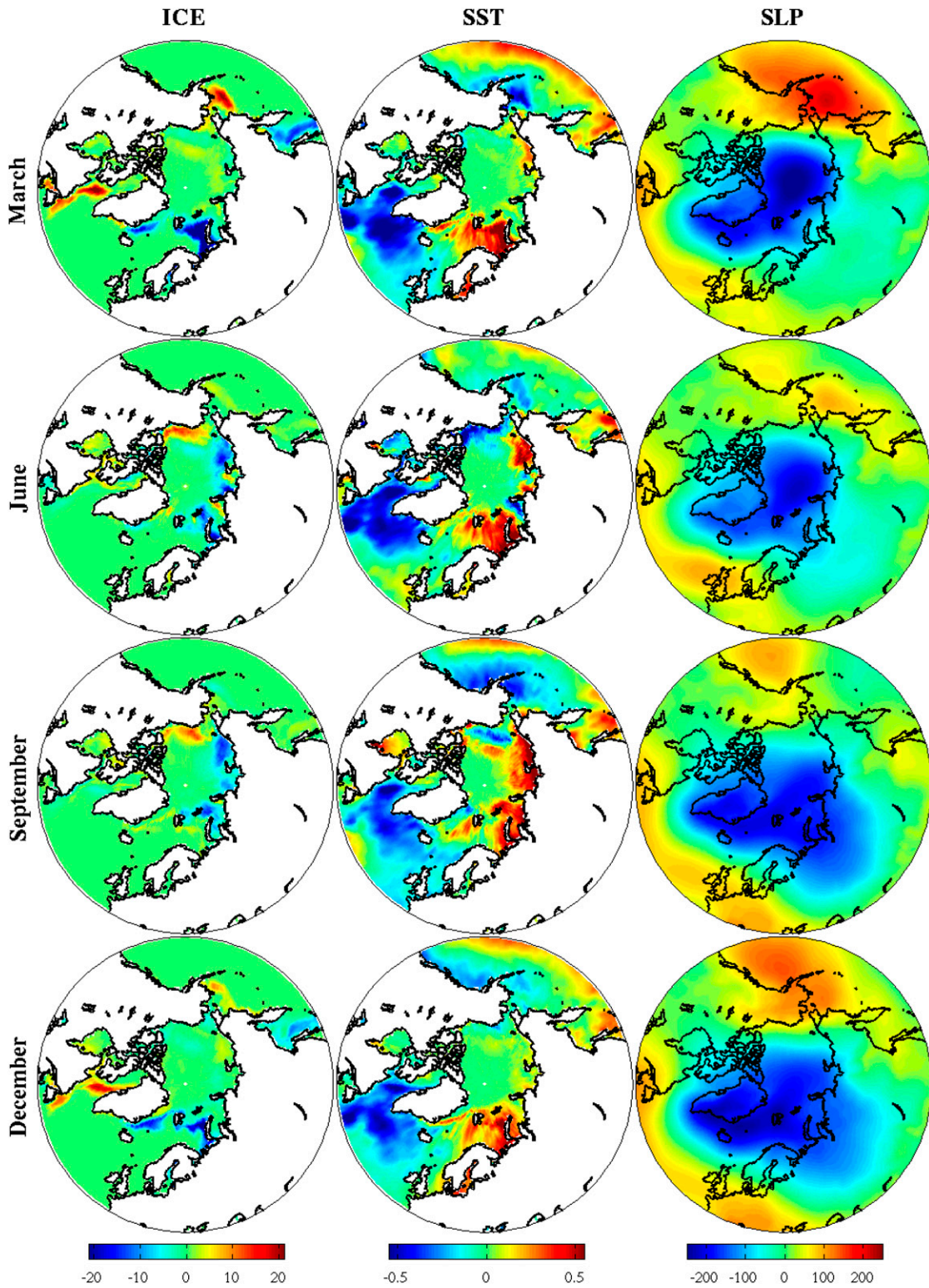


FIG. 15. Sea ice, SST, and SLP patterns of HadISST reemergence family \mathcal{F}_1^0 shown for different months of 1991.

anomalies begin to reappear with the same sign and a similar spatial pattern to the previous winter. This coincides with the beginning of the sea ice growth season and the reemergence of ice anomalies from the previous spring. In December, we observe a strong dipole SLP anomaly, and, again, observe sea ice anomalies in the Bering, Barents–Kara, and Labrador Seas, which are physically consistent with this pattern.

Besides explaining the observed teleconnection in sea ice anomalies, these SLP patterns also suggest an SLP–sea ice reemergence mechanism via their winter-to-winter regime persistence. Mode L_3^{SLP} , the low-frequency SLP mode of \mathcal{F}_1^M , has a strong 1-yr autocorrelation of 0.70. Because SLP anomalies produce a significant sea ice response, recurring SLP patterns will produce recurring sea ice patterns. Thus, the observed winter-to-winter persistence of the SLP patterns of \mathcal{F}_1^M provides a candidate mechanism for sea ice reemergence.

As mentioned earlier, in [section 4c](#), the SLP patterns of \mathcal{F}_1^M represent a low-pass-filtered version of the full atmospheric signal. The SLP patterns of \mathcal{F}_1^M should be thought of as a slowly evolving atmospheric circulation regime, rather than a snapshot of the full SLP field at each point in time. For example, the temporal evolution of the full SLP field is similar to the time series of PC_1^{SLP} in [Fig. 8](#), whereas the SLP patterns of \mathcal{F}_1^M are similar to the low-pass-filtered PC (red curve in [Fig. 8](#)). It is the persistence of the atmospheric circulation regime of \mathcal{F}_1^M that provides a plausible mechanism for sea ice reemergence. Sea ice anomalies are known to have a persistence of 2–5 months ([Blanchard-Wrigglesworth et al. 2011](#)); therefore, the sea ice anomalies at a given time represent an integrated response to earlier atmospheric and oceanic forcing. Given this, one would expect that sea ice anomalies are not strongly dependent on the chaotic month-to-month fluctuations of the atmosphere but are more dependent on a temporally smoothed version of this fluctuating field. Therefore, the low-pass filtered SLP patterns of \mathcal{F}_1^M provide a plausible physical link between atmospheric and sea ice variability. The study of [Blanchard-Wrigglesworth et al. \(2011\)](#) dismisses SLP persistence as a source of sea ice reemergence because of the low 1-month autocorrelation of the SLP pattern that best explains changes in sea ice extent. Here, we argue that the low-frequency component of similar SLP patterns may play an important role in sea ice reemergence.

Similar relationships between sea ice and SLP anomalies are also observed in family \mathcal{F}_2^M ([Fig. 14](#)), which has an annular SLP pattern resembling the AO and a 1-yr autocorrelation of 0.41. Similar to \mathcal{F}_1^M , these SLP patterns are strongly active over the winter months (October–March) and fairly inactive over the summer

months. The geostrophic winds of this pattern are primarily zonal but also have a meridional component, which affects sea ice via surface air temperature advection. In January–March, there are northeasterly winds over the Bering Sea, southeasterly winds over Labrador Sea, and northeasterly winds over the Barents–Kara Seas, with corresponding positive, negative, and positive sea ice anomalies, respectively. The SLP anomalies become small over the summer months and reappear during the fall months with the same sign as the previous winter. With the reappearance of these SLP anomalies, we observe an ice reemergence, which is particularly strong in the Bering and Labrador Seas.

The relationship between SLP and sea ice is somewhat less clear in the observations than in the model. The right panels of [Fig. 15](#) show the \mathcal{F}_1^O SLP patterns for 1991, a year when the family was active. In January–March, there is an AO-like SLP pattern producing northerly winds over the Labrador Sea and southerly winds over the Barents–Kara Seas. We observe corresponding positive and negative sea ice anomalies in these seas, analogous to what was observed in \mathcal{F}_2^M . However, the SLP patterns differ in the North Pacific. There is minimal advection over the Bering Sea, as a high pressure anomaly is centered directly over it. This anomaly produces southerly winds over the Sea of Okhotsk, which are consistent with the negative sea ice anomaly. On the other hand, the SLP patterns do not provide a clear explanation, in terms of meridional wind, for the positive Bering sea ice anomalies. Compared to \mathcal{F}_2^M , these SLP patterns do not decorrelate as strongly over the summer months, and a negative SLP anomaly is retained over the pole, which also shifts onto the Eurasian continent over the summer months. The anomaly strengthens during the fall, producing similar winds and sea ice patterns to the previous winter. One notable difference between the observational and model SLP families is the spatial stationarity of the SLP patterns. The SLP patterns of \mathcal{F}_1^M and \mathcal{F}_2^M are relatively fixed in space and pulse on and off with the annual cycle. The \mathcal{F}_1^O SLP patterns also pulse with the annual cycle but are transient in space. The SLP centers of action advect substantially over the course of a year.

Given the seemingly similar sea ice anomalies of \mathcal{F}_1^M and \mathcal{F}_1^O , a natural question is why these families have such different atmospheric patterns. A closer analysis of the sea ice variability of each family reveals clear differences between the two. For each family, we compute the proportion of sea ice variance in a given region, relative to the variance of the full Arctic domain. We find that \mathcal{F}_1^M contains 24% of its variance in the Bering Sea, 22% in the Barents–Kara Seas, and 8% in the Labrador Sea. Conversely, \mathcal{F}_1^O contains 5% of its variance

in the Bering Sea, 35% in the Barents–Kara Seas, and 14% in the Labrador Sea. Therefore, the dominant sea ice feature of \mathcal{F}_1^M is the dipole between the Bering and Barents–Kara Seas, whereas the dominant feature of \mathcal{F}_1^O is the dipole between the Labrador and Barents–Kara Seas. The corresponding atmospheric circulation patterns of each family act to reinforce these dominant sea ice anomalies and have significantly different spatial patterns.

It should be noted that the data analysis approach employed here is capable of identifying correlation but not causality. In particular, we have not quantified the relative importance of the ocean and the atmosphere in producing sea ice reemergence. Also, we have identified SLP modes with interannual to decadal variability but have not provided a mechanism for this observed variability. We speculate that, rather than intrinsic atmospheric variability, this low-frequency variability of the atmosphere results from SST or sea ice forcing. The generation of low-frequency atmospheric variability has been widely studied, with many authors suggesting that extratropical and tropical SST anomalies are capable of driving low-frequency variability in the atmosphere (Lau and Nath 1990; Latif and Barnett 1994; Trenberth and Hurrell 1994; Weng and Neelin 1998; Selten et al. 1999; Robertson et al. 2000; Kushnir et al. 2002; Czaja and Frankignoul 2002). Other authors (e.g., Mysak and Venegas 1998) have suggested that sea ice anomalies could drive low-frequency atmospheric patterns, but modeling studies have suggested that the atmospheric response is quite weak compared with the typical magnitude of atmospheric anomalies (Alexander et al. 2004; Magnusdottir et al. 2004). Therefore, we speculate that anomalous SST forcing is the most likely candidate for the observed low-frequency SLP patterns, but more study is required on this problem. These unanswered questions could be investigated in a future study involving a hierarchy of GCM experiments.

c. Metrics for sea ice reemergence

We now establish a set of reemergence metrics for sea ice, SST, and SLP, by which one can judge the activity of sea ice reemergence and associated mechanisms in different regions. These metrics, computed for the reconstructed fields of each family, quantify the intensity and sign of ice reemergence events. We focus on the values of these metrics in the Bering, Barents–Kara, and Labrador Seas. The sea ice metric is defined as the integrated (area weighted) SIC anomaly in a given region. We define the SLP metric as the maximum value of the meridional geostrophic wind over a given region. This is a proxy for the amount of warm/cold air advection and northward/southward ice advection over a given region. The SST metric is defined as the integrated (area weighted) SST

anomalies in the portion of the seas that are imprinted by summer SST anomalies. Specifically, we compute the integrated SST anomalies in the Kara Sea (65°–80°N, 75°–100°E), the northern Bering Sea (60°–65°N, 165°E–160°W), and the northern Labrador Sea (60°–80°N, 70°–40°W). It is helpful to compare the metrics, plotted in Figs. 16–18, to movies 5–7 in the online supplementary material which show the dynamical evolution of the corresponding fields for the same time period.

Figure 16 shows \mathcal{F}_1^M metrics for 100 yr of model output. We observe a number of reemergence events, characterized by periods in which the sea ice metric is large, with consistent sign, over a number of successive winters. For example, notable periods of active reemergence occur during years 101–106, 128–131, 146–155, and 175–179. The sea ice phase relationships for this family are striking, with strong positive correlation (0.95) between the Bering and Labrador Seas and strong anticorrelation (–0.95) between the Bering and Barents–Kara Seas. The SST metric reveals the SST–sea ice reemergence mechanism, as years with large ice metrics have large SST metrics of the opposite sign (note the anticorrelation of like-colored curves in Figs. 16a,b). During reemergence events, the SST metrics are close to zero in the winter months and grow large in the summer months as the sea ice anomalies imprint the SST field. These SST metrics also show a clear in-phase relationship between the Bering and Labrador Seas and out-of-phase relationship between the Bering and Barents–Kara Seas. The SLP metric is clearly out of phase with the sea ice metric, which illustrates the sea ice–SLP reemergence mechanism, since positive (negative) meridional wind anomalies produce negative (positive) sea ice anomalies. During reemergence events, in the Bering and Labrador Seas, we observe that the SLP metric is large over the winter and close to zero over the summer. In the Barents–Kara Seas, we observe more persistence, as the family maintains its wind anomalies throughout an entire reemergence event.

Figure 17 shows the metrics for family \mathcal{F}_2^M . Again, we observe very strong phase relationships in sea ice anomalies, with in-phase anomalies between the Barents–Kara and Bering Seas and out-of-phase anomalies between the Bering and Labrador Seas. The SST metric displays strong SST–sea ice reemergence mechanisms in the Labrador and Bering Seas. Also, as noted in section 5c, there is not a clear SST–sea ice mechanism in the Barents–Kara Seas. The SLP metric has a strong signal in the Labrador Sea, which is large in winter and small in summer and out of phase with the sea ice anomalies. The SLP–sea ice mechanism is less strong in the Barents–Kara and Bering Seas, yet we do observe persistent wind anomalies that are out of phase with the sea ice anomalies.

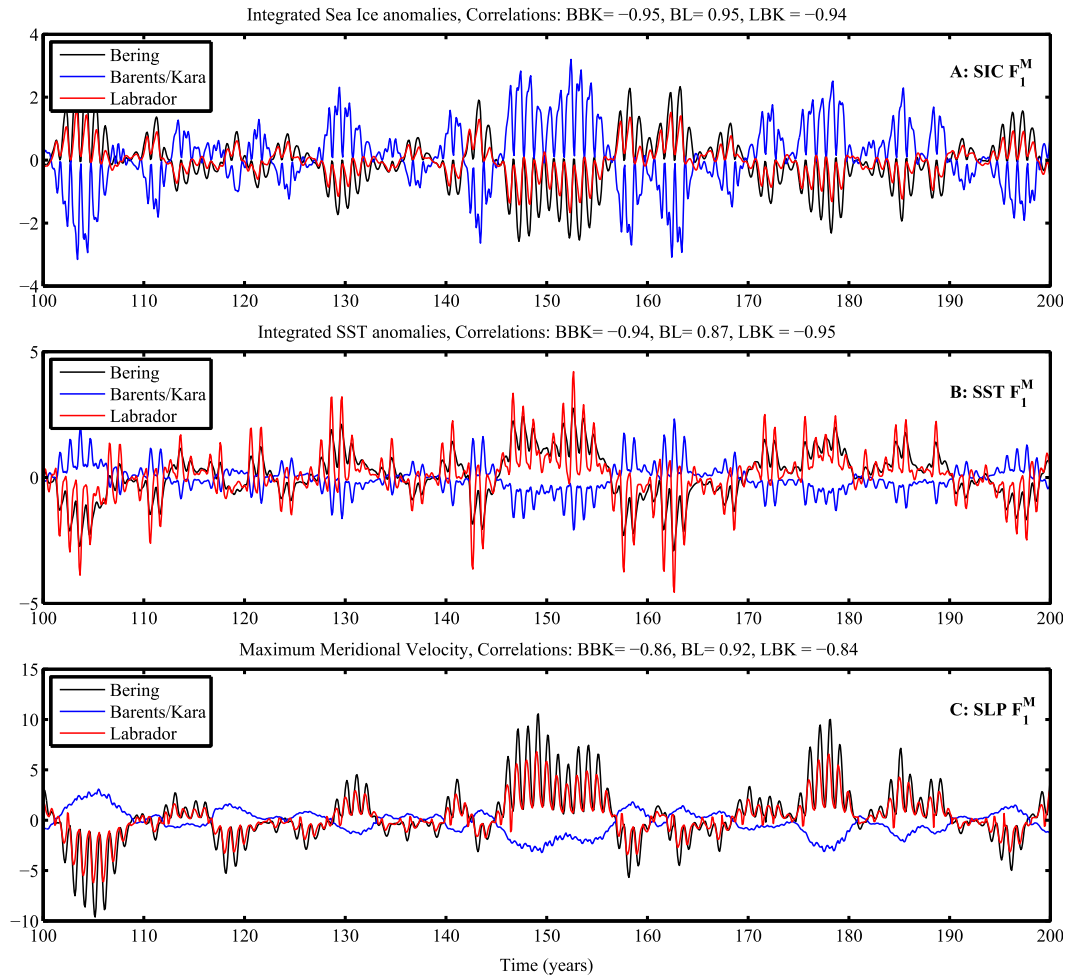


FIG. 16. Reemergence metrics for sea ice, SST, and wind of family \mathcal{F}_1^M in the Barents–Kara, Bering, and Labrador Seas, by which we judge the activity of ice reemergence. Active periods of reemergence are characterized by repeated years in which these metrics are large (either positive or negative). Note that the SIC and SST metrics have been normalized by their respective standard deviations and the SLP metric is reported in meters per second.

We show metrics for \mathcal{F}_1^O in Fig. 18. This family exhibits a strong SST–sea ice reemergence mechanism in the Barents–Kara Seas. The SST signal is very weak in the Bering Sea, and in the Labrador Sea it tends to persist over periods of reemergence, rather than being imprinted each summer. The wind anomalies in the Labrador and Barents–Kara Seas are consistent with the sea ice–SLP reemergence mechanism. As noted earlier, the Bering Sea wind anomalies are not consistent with the sea ice anomalies. Rather, we observe that the wind anomalies are inconsistent (in phase) with the sea ice anomalies.

d. Regional sea ice relationships conditional on SLP modes

The reemergence families suggest a number of sea ice teleconnections that are related to large-scale SLP patterns. Are these regional teleconnections visible in the

raw SIC data? Are the teleconnections strengthened by conditioning on certain low-frequency SLP modes being active? To answer these questions, we select pairs of regions and compute lagged cross correlations in total sea ice area anomalies of the raw data between these regions. Note that the cross correlations are obtained by computing a time series of sea ice area anomalies for each region and performing lagged correlations between these two time series. Our choice of regions and SLP modes is guided by the reemergence families. We consider the regions and SLP pattern that display the strongest teleconnection for each family.

The results are shown in Fig. 19, for months of the year with sea ice coverage in the marginal ice zones (December–May) and for lags from -23 to 23 months. Figures 19a,b show lagged cross correlations between the Barents–Kara and Bering Seas for the raw CCSM3 data and conditional

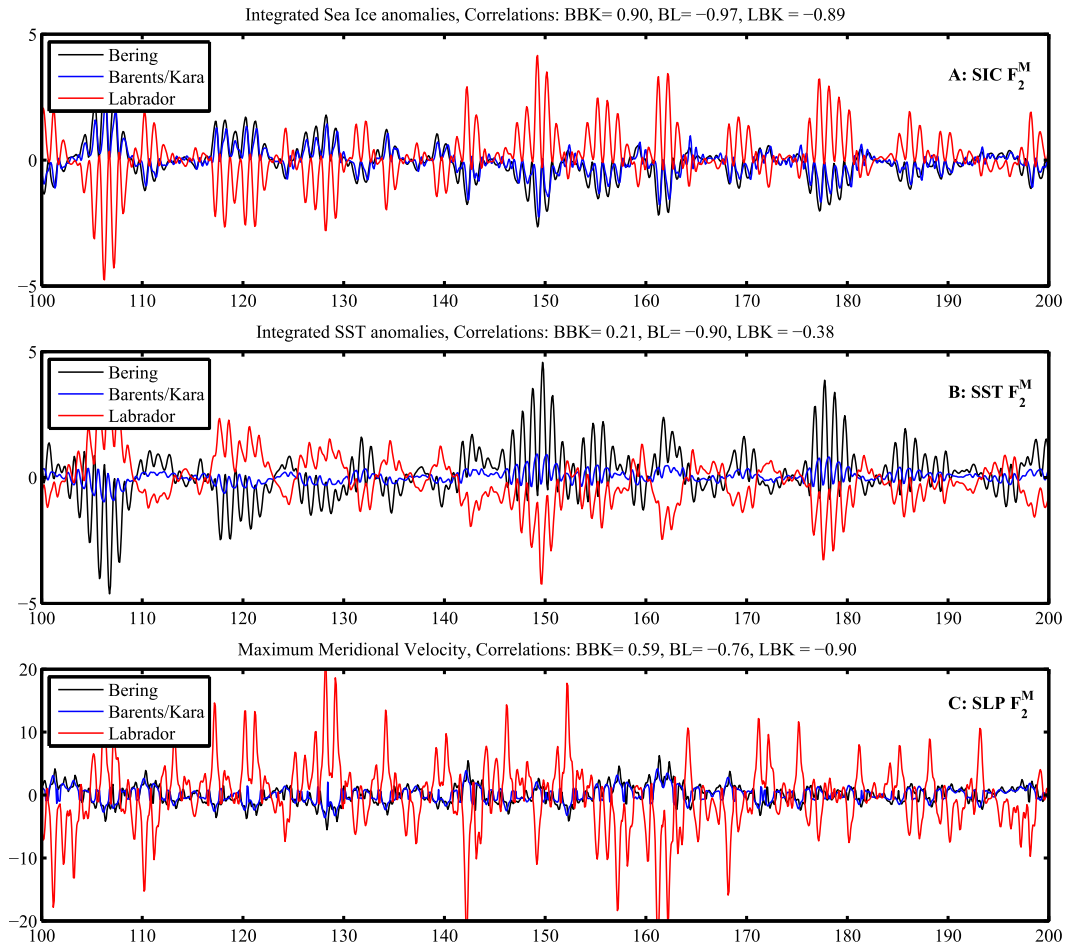


FIG. 17. As in Fig. 16, but for the family \mathcal{F}_2^M .

on $|L_3^{\text{SLP}}| > 1.5$ (corresponds to 14% of the data), respectively. This corresponds to the primary teleconnection of \mathcal{F}_1^M . All correlations plotted in color are significant at the 95% level, based on a t -distribution statistic. In the raw data, we observe negative correlations between the Bering and Barents–Kara Seas, which are strongest at lags from -6 to 6 months. There is a dramatic strengthening of these negative correlations when conditioned on an active L_3^{SLP} mode (the DA mode). We also observe that the correlations are more persistent when the DA mode is active. Another interesting feature is the clear bias in correlations toward lags in which Bering Sea anomalies lead anomalies in the Barents–Kara Seas. The analogous correlations, corresponding to family \mathcal{F}_2^M , are shown in Figs. 19c,d for the Labrador and Bering Seas and for SLP mode L_1^{SLP} (the AO mode). These correlations are very small compared with Figs. 19a,b. The raw data display very little correlation structure, and weak correlations, which are primarily negative, emerge after conditioning on the AO mode. It should be noted that the

limb of negative correlations, with Bering lagging Labrador, corresponds to summer sea ice anomalies in the Bering Sea, which are extremely weak. Therefore, this limb has questionable significance.

Figures 19e,f show cross correlations between the Barents–Kara and Labrador Seas for the HadISST, conditional on $|L_1^{\text{SLP}}| > 1$ (corresponds to 35% of the data). Note that we use a value of 1 rather than 1.5 for the conditional correlations because of the shortness of the observational time series. Also, the shortness of the time series implies a higher 95% significance level for correlations. We plot correlations using the same color bar as CCSM3 and simply white out all correlations that are not significant at the 95% level. The raw data display some negative correlation, but a dramatic strengthening is observed when conditioning on an active AO mode. The limb of white in Fig. 19f, extending from May (+3) to December (+9) corresponds to lagged correlations with summer months. At lags beyond this limb, we observe strong negative correlations. This feature is

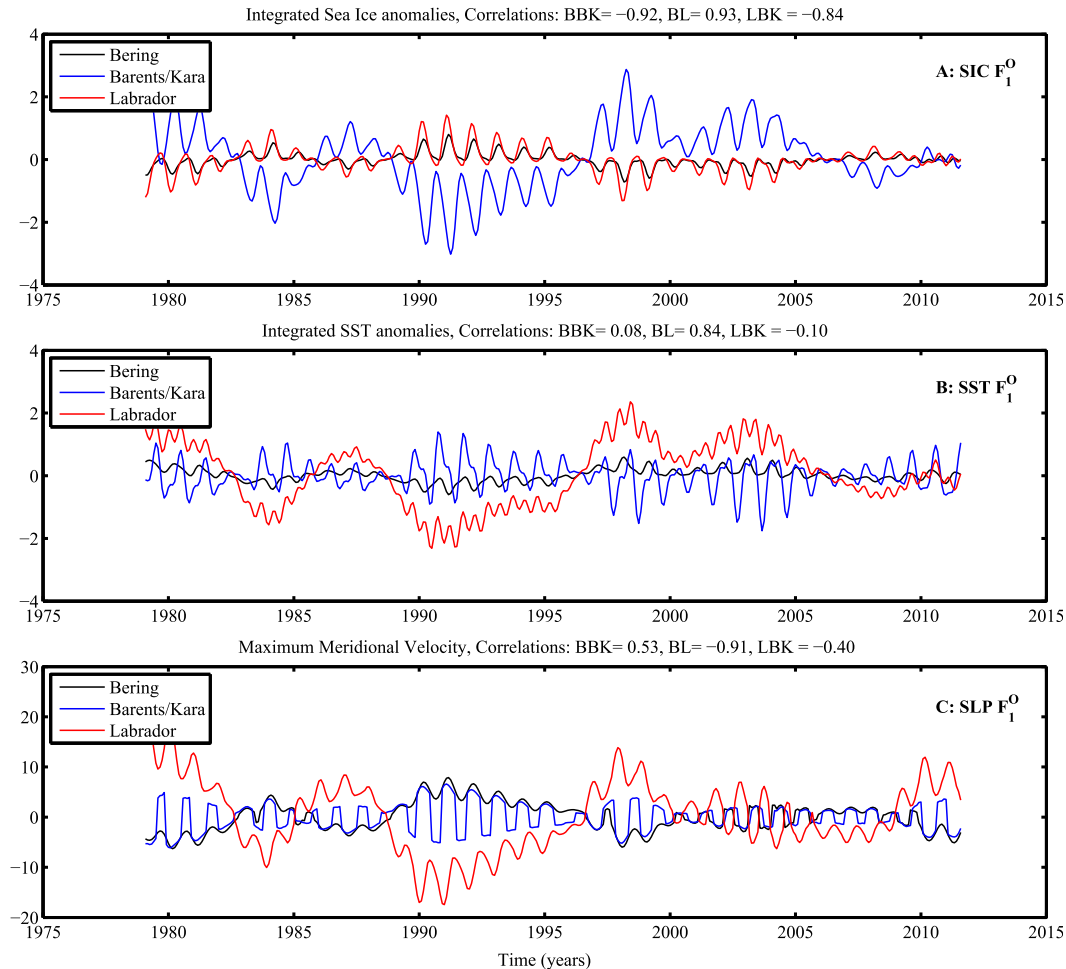


FIG. 18. As in Fig. 16, but for the family \mathcal{F}_1^O .

a reemergence of anticorrelation between the Barents–Kara and Labrador Seas. The reemergence structure is less clear for negative lags, where the Labrador Sea leads the Barents–Kara Seas; however, we generally observe anticorrelation between the two seas, which is significantly stronger than in the raw data.

7. Conclusions

We have studied Arctic sea ice reemergence (Blanchard-Wrigglesworth et al. 2011) in a comprehensive climate model and observations. This study has documented the regional and temporal details of sea ice reemergence and illustrated two potential reemergence mechanisms, involving SST and SLP persistence, respectively. We have used coupled NLSA (Giannakis and Majda 2012b, 2013; Bushuk et al. 2014), a nonlinear data analysis technique for multivariate time series, to analyze the covariability of Arctic SIC, SST, and SLP. Coupled NLSA was applied to a 900-yr-equilibrated

control integration of CCSM3, yielding spatiotemporal modes, analogous to EEOFs, and temporal patterns, analogous to PCs. Modes were also extracted from 34 years of observational data, using SIC and SST observations from HadISST and SLP reanalysis from ERA-Interim. In both the model and observations, these NLSA modes capture three distinct types of temporal behavior: periodic, low-frequency, and intermittent variability. The low-frequency modes have spatial patterns that closely resemble the leading EOFs of each variable. In particular, the low-frequency SLP modes correlate strongly with the well-known Arctic Oscillation (AO; Thompson and Wallace 1998) and Arctic dipole anomaly (DA; Wu et al. 2006) patterns of SLP variability. The temporal patterns of the low-frequency SLP modes, obtained here without any preprocessing of the raw data, closely resemble a low-pass-filtered version of the corresponding PCs obtained via EOF analysis.

Performing time-lagged pattern correlations, we have found clear pan-Arctic sea ice reemergence signals in the model and observations. The lagged pattern

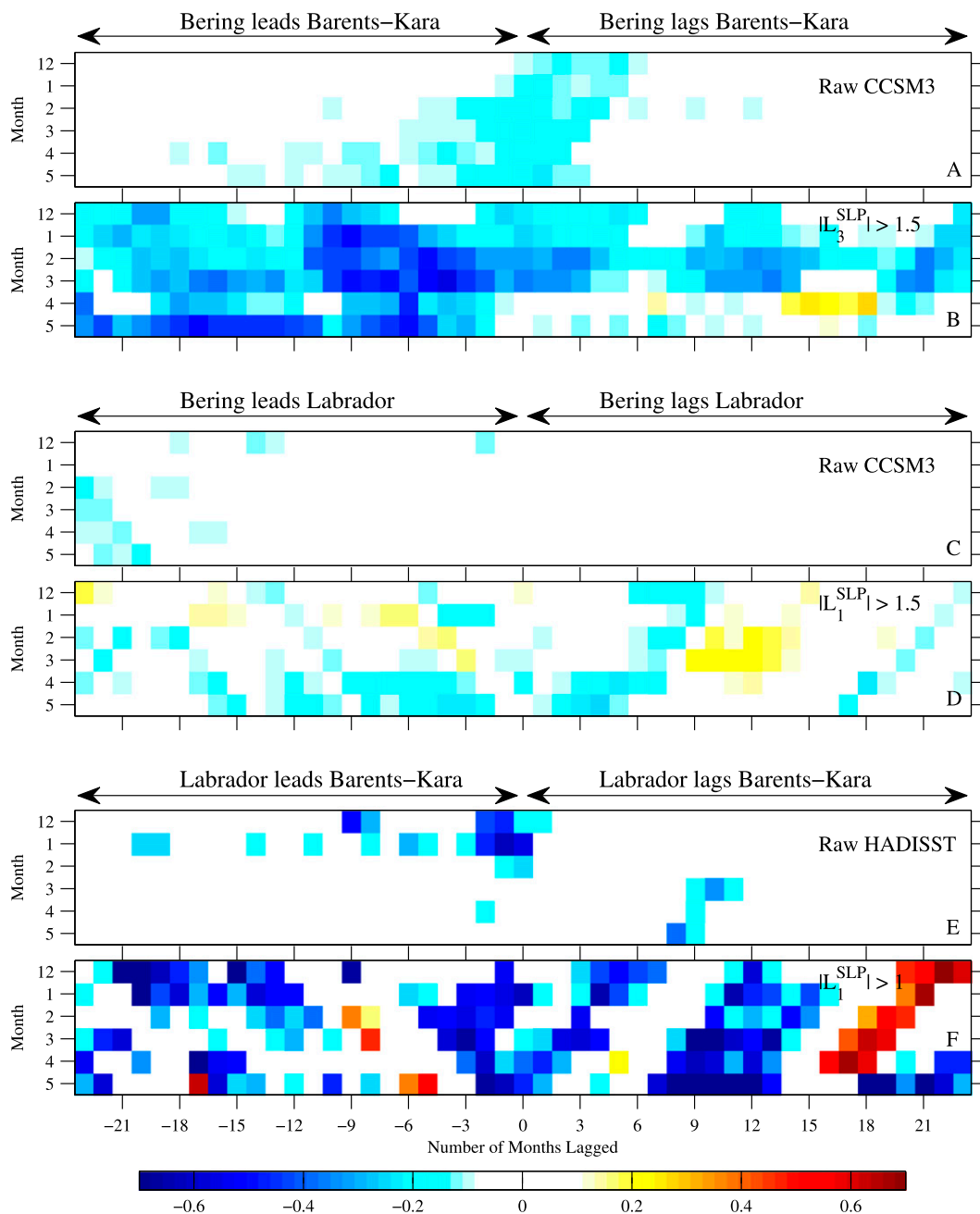


FIG. 19. Lagged correlations in sea ice area anomalies between different seas: shown are CCSM3 correlations between the Barents–Kara and Bering Seas for (a) the raw data and (b) conditional on $|L_3^{\text{SLP}}| > 1.5$, CCSM3 correlations between the Bering and Labrador Seas for (c) the raw data and (d) conditional on $|L_1^{\text{SLP}}| > 1.5$, and HADISST correlations between the Barents–Kara and Labrador Seas for (e) the raw data and (f) conditional on $|L_1^{\text{SLP}}| > 1$.

correlation approach employed in this study reveals a stronger reemergence signal in observations than previous studies on reemergence (Blanchard-Wrigglesworth et al. 2011; Day et al. 2014). Using coupled NLSA modes, we have found low-dimensional families that are able to reproduce the reemergence signal of the raw SIC

data. Intriguingly, these families explain a relatively small portion of the raw SIC variance, yet when removed from the raw data the resulting signal exhibits significantly weaker reemergence. Moreover, the associated SST and SLP patterns of these families demonstrate two possible reemergence mechanisms, consistent

with those proposed by Blanchard-Wrigglesworth et al. (2011) and Deser et al. (2002). The SST–sea ice reemergence mechanism, in which spring sea ice anomalies are imprinted and stored as summer SST anomalies, is clearly active in the Barents–Kara, Bering, and Labrador Seas. The SLP–sea ice mechanism, in which sea ice anomalies reemerge because of the winter-to-winter persistence of low-pass-filtered SLP anomalies (atmospheric regimes), is also observed in these regions, with the exception of the Bering Sea in the observational record.

A key finding of this study is that these reemergence patterns are part of a pan-Arctic-scale organization involving SLP teleconnection patterns. In particular, we have found strong phase relationships between sea ice reemergence events in geographically distinct regions. Unable to explain this teleconnection in terms of purely local SST anomalies, we find clear relationships between regional sea ice anomalies and large-scale SLP variability. In CCSM3, an out-of-phase relationship between the Bering/Labrador and Barents–Kara Seas is found to be consistent with the phase and amplitude of the DA mode. Similarly, an out-of-phase relationship between the Bering/Barents–Kara and Labrador Seas is found to be consistent with the phase and amplitude of the AO mode. In observations, the AO mode is able to explain the strong out-of-phase anomalies of the Barents–Kara and Labrador Seas but cannot explain the weaker anomalies of the Bering Sea. These regional phase relationships are weakly visible in the raw SIC data and are significantly strengthened by conditioning on an appropriate SLP mode (the AO or DA) being active.

Another key aspect of this study is the regional and temporal characterization of sea ice reemergence. We have identified significant regional differences in reemergence between the model and observations, particularly in the Labrador Sea and the North Pacific sector, despite their pan-Arctic agreement. We have also found that reemergence events and mechanisms have significant temporal variability, and that the low-frequency modes of the reemergence families act as effective predictors of periods of active or quiescent reemergence. A set of reemergence metrics has been created, by which one can judge the strength and sign of sea ice reemergence events and the associated SST and SLP mechanisms.

In this study, we have demonstrated two plausible mechanisms for sea ice reemergence, involving the atmosphere and the ocean, but which mechanism is most crucial in producing ice reemergence? Is sea ice reemergence a fully coupled phenomenon, or does it also occur in more idealized situations? This data analysis study has identified correlation but not causation. An interesting subject for future work would be to perform a suite of coupled model experiments to study this question of causality.

Acknowledgments. We thank Ed Blanchard-Wrigglesworth and two anonymous reviewers for valuable comments that helped improve the manuscript. D. Giannakis and A. J. Majda wish to acknowledge support from ONR MURI Grant 25-74200-F7112. The research of D. Giannakis is partially supported by ONR DRI Grant N00014-14-1-0150. M. Bushuk is supported as a graduate student under this grant. M. Bushuk also received support from the Center for Prototype Climate Modeling at NYU Abu Dhabi Research Institute and NSERC PGS-D Award 404213.

REFERENCES

- Alexander, M. A., C. Deser, and M. S. Timlin, 1999: The reemergence of SST anomalies in the North Pacific Ocean. *J. Climate*, **12**, 2419–2433, doi:10.1175/1520-0442(1999)012<2419:TROSAI>2.0.CO;2.
- , U. S. Bhatt, J. E. Walsh, M. S. Timlin, J. S. Miller, and J. D. Scott, 2004: The atmospheric response to realistic Arctic sea ice anomalies in an AGCM during winter. *J. Climate*, **17**, 890–905, doi:10.1175/1520-0442(2004)017<0890:TARTRA>2.0.CO;2.
- Aubry, N., W.-Y. Lian, and E. S. Titi, 1993: Preserving symmetries in the proper orthogonal decomposition. *SIAM J. Sci. Comput.*, **14**, 483–505, doi:10.1137/0914030.
- Berry, T., R. Cressman, Z. Greguric-Ferencek, and T. Sauer, 2013: Time-scale separation from diffusion-mapped delay coordinates. *SIAM J. Appl. Dyn. Syst.*, **12**, 618–649, doi:10.1137/12088183X.
- Blanchard-Wrigglesworth, E., K. C. Armour, C. M. Bitz, and E. DeWeaver, 2011: Persistence and inherent predictability of Arctic sea ice in a GCM ensemble and observations. *J. Climate*, **24**, 231–250, doi:10.1175/2010JCLI3775.1.
- Broomhead, D. S., and G. P. King, 1986: Extracting qualitative dynamics from experimental data. *Physica D*, **20** (2–3), 217–236, doi:10.1016/0167-2789(86)90031-X.
- Bushuk, M., D. Giannakis, and A. J. Majda, 2014: Reemergence mechanisms for North Pacific sea ice revealed through nonlinear Laplacian spectral analysis. *J. Climate*, **27**, 6265–6287, doi:10.1175/JCLI-D-13-00256.1.
- Cavaleri, D. J., and C. L. Parkinson, 2012: Arctic sea ice variability and trends, 1979–2010. *Cryosphere*, **6**, 881–889, doi:10.5194/tc-6-881-2012.
- Collins, W. D., and Coauthors, 2004: Description of the NCAR Community Atmosphere Model (CAM 3.0). National Center for Atmospheric Research Tech. Rep. TN-464+STR, 226 pp.
- , and Coauthors, 2006: The Community Climate System Model version 3 (CCSM3). *J. Climate*, **19**, 2122–2143, doi:10.1175/JCLI3761.1.
- Czaja, A., and C. Frankignoul, 2002: Observed impact of Atlantic SST anomalies on the North Atlantic Oscillation. *J. Climate*, **15**, 606–623, doi:10.1175/1520-0442(2002)015<0606:OIOASA>2.0.CO;2.
- Day, J., S. Tietsche, and E. Hawkins, 2014: Pan-Arctic and regional sea ice predictability: Initialization month dependence. *J. Climate*, **27** (12), 4371–4390, doi:10.1175/JCLI-D-13-00614.1.
- de Coëtlogon, G., and C. Frankignoul, 2003: On the persistence of winter sea surface temperature in the North Atlantic. *J. Climate*, **16**, 1364–1377, doi:10.1175/1520-0442-16.9.1364.

- Dee, D. P., and Coauthors, 2011: The ERA-Interim reanalysis: Configuration and performance of the data assimilation system. *Quart. J. Roy. Meteor. Soc.*, **137**, 553–597, doi:10.1002/qj.828.
- Deser, C., J. E. Walsh, and M. S. Timlin, 2000: Arctic sea ice variability in the context of recent atmospheric circulation trends. *J. Climate*, **13**, 617–633, doi:10.1175/1520-0442(2000)013<0617:ASIVIT>2.0.CO;2.
- , M. Holland, G. Reverdin, and M. S. Timlin, 2002: Decadal variations in Labrador sea ice cover and North Atlantic sea surface temperatures. *J. Geophys. Res.*, **107**, doi:10.1029/2000JC000683.
- Francis, J. A., and E. Hunter, 2007: Drivers of declining sea ice in the Arctic winter: A tale of two seas. *Geophys. Res. Lett.*, **34**, L17503, doi:10.1029/2007GL030995.
- Ghil, M., and Coauthors, 2002: Advanced spectral methods for climatic time series. *Rev. Geophys.*, **40**, 1003, doi:10.1029/2000RG000092.
- Giannakis, D., and A. J. Majda, 2012a: Comparing low-frequency and intermittent variability in comprehensive climate models through nonlinear Laplacian spectral analysis. *Geophys. Res. Lett.*, **39**, L10710, doi:10.1029/2012GL051575.
- , and —, 2012b: Nonlinear Laplacian spectral analysis for time series with intermittency and low-frequency variability. *Proc. Natl. Acad. Sci. USA*, **109**, 2222–2227, doi:10.1073/pnas.1118984109.
- , and —, 2013: Nonlinear Laplacian spectral analysis: Capturing intermittent and low-frequency spatiotemporal patterns in high-dimensional data. *Stat. Anal. Data Min.*, **6**, 180–194, doi:10.1002/sam.11171.
- , and —, 2014: Data-driven methods for dynamical systems: Quantifying predictability and extracting spatiotemporal patterns. *Mathematical and Computational Modeling: With Applications in Engineering and the Natural and Social Sciences*, R. Melnik, Ed., Wiley, 137–191.
- Holland, M. M., C. Bitz, E. Hunke, W. Lipscomb, and J. Schramm, 2006: Influence of the sea ice thickness distribution on polar climate in CCSM3. *J. Stat. Phys.*, **19**, 2398–2414.
- Johnson, M. A., A. Y. Proshutinsky, and I. V. Polyakov, 1999: Atmospheric patterns forcing two regimes of Arctic circulation: A return to anticyclonic conditions? *Geophys. Res. Lett.*, **26**, 1621–1624, doi:10.1029/1999GL900288.
- Kay, J. E., M. M. Holland, and A. Jahn, 2011: Inter-annual to multi-decadal Arctic sea ice extent trends in a warming world. *Geophys. Res. Lett.*, **38**, L15708, doi:10.1029/2011GL048008.
- Kushnir, Y., W. Robinson, I. Bladé, N. Hall, S. Peng, and R. Sutton, 2002: Atmospheric GCM response to extratropical SST anomalies: Synthesis and evaluation. *J. Climate*, **15**, 2233–2256, doi:10.1175/1520-0442(2002)015<2233:AGRTES>2.0.CO;2.
- Latif, M., and T. P. Barnett, 1994: Causes of decadal climate variability over the North Pacific and North America. *Science*, **266**, 634–637, doi:10.1126/science.266.5185.634.
- Lau, N.-C., and M. J. Nath, 1990: A general circulation model study of the atmospheric response to extratropical SST anomalies observed in 1950–79. *J. Climate*, **3**, 965–989, doi:10.1175/1520-0442(1990)003<0965:AGCMSO>2.0.CO;2.
- L’Heureux, M. L., A. Kumar, G. D. Bell, M. S. Halpert, and R. W. Higgins, 2008: Role of the Pacific-North American (PNA) pattern in the 2007 Arctic sea ice decline. *Geophys. Res. Lett.*, **35**, L20701, doi:10.1029/2008GL035205.
- Magnusdottir, G., C. Deser, and R. Saravanan, 2004: The effects of North Atlantic SST and sea ice anomalies on the winter circulation in CCM3. Part I: Main features and storm track characteristics of the response. *J. Climate*, **17**, 857–876, doi:10.1175/1520-0442(2004)017<0857:TEONAS>2.0.CO;2.
- Maslanik, J., S. Drobot, C. Fowler, W. Emery, and R. Barry, 2007: On the Arctic climate paradox and the continuing role of atmospheric circulation in affecting sea ice conditions. *Geophys. Res. Lett.*, **34**, L03711, doi:10.1029/2006GL028269.
- Moritz, R. E., C. M. Bitz, and E. J. Steig, 2002: Dynamics of recent climate change in the Arctic. *Science*, **297**, 1497–1502, doi:10.1126/science.1076522.
- Mysak, L. A., and S. A. Venegas, 1998: Decadal climate oscillations in the Arctic: A new feedback loop for atmosphere-ice-ocean interactions. *Geophys. Res. Lett.*, **25**, 3607–3610, doi:10.1029/98GL02782.
- Overland, J. E., and M. Wang, 2005: The third Arctic climate pattern: 1930s and early 2000s. *Geophys. Res. Lett.*, **32**, L23808, doi:10.1029/2005GL024254.
- , and —, 2010: Large-scale atmospheric circulation changes are associated with the recent loss of Arctic sea ice. *Tellus*, **62A**, 1–9, doi:10.1111/j.1600-0870.2009.00421.x.
- Polyakov, I. V., and M. A. Johnson, 2000: Arctic decadal and interdecadal variability. *Geophys. Res. Lett.*, **27**, 4097–4100, doi:10.1029/2000GL011909.
- Proshutinsky, A. Y., and M. A. Johnson, 1997: Two circulation regimes of the wind-driven Arctic Ocean. *J. Geophys. Res.*, **102** (C6), 12 493–12 514, doi:10.1029/97JC00738.
- Rayner, N. A., D. E. Parker, E. B. Horton, C. K. Folland, L. V. Alexander, D. P. Rowell, E. C. Kent, and A. Kaplan, 2003: Global analyses of sea surface temperature, sea ice, and night marine air temperature since the late nineteenth century. *J. Geophys. Res.*, **108**, 4407, doi:10.1029/2002JD002670.
- Rigor, I. G., and J. M. Wallace, 2004: Variations in the age of Arctic sea-ice and summer sea-ice extent. *Geophys. Res. Lett.*, **31**, L09401, doi:10.1029/2004GL019492.
- , —, and R. L. Colony, 2002: Response of sea ice to the Arctic Oscillation. *J. Climate*, **15**, 2648–2663, doi:10.1175/1520-0442(2002)015<2648:ROSITT>2.0.CO;2.
- Robertson, A. W., C. R. Mechoso, and Y.-J. Kim, 2000: The influence of Atlantic sea surface temperature anomalies on the North Atlantic Oscillation. *J. Climate*, **13**, 122–138, doi:10.1175/1520-0442(2000)013<0122:TIOASS>2.0.CO;2.
- Screen, J. A., I. Simmonds, and K. Keay, 2011: Dramatic inter-annual changes of perennial Arctic sea ice linked to abnormal summer storm activity. *J. Geophys. Res.*, **116**, D15105, doi:10.1029/2011JD015847.
- Selten, F. M., R. Haarsma, and J. Opsteegh, 1999: On the mechanism of North Atlantic decadal variability. *J. Climate*, **12**, 1956–1973, doi:10.1175/1520-0442(1999)012<1956:OTMONA>2.0.CO;2.
- Serreze, M. C., and Coauthors, 2003: A record minimum arctic sea ice extent and area in 2002. *Geophys. Res. Lett.*, **30**, 1110, doi:10.1029/2002GL016406.
- , M. M. Holland, and J. Stroeve, 2007: Perspectives on the Arctic’s shrinking sea-ice cover. *Science*, **315**, 1533–1536, doi:10.1126/science.1139426.
- Smith, R., and P. Gent, 2004: Reference manual for the Parallel Ocean Program (POP): Ocean component of the Community Climate System Model (CCSM2.0 and 3.0). Los Alamos National Laboratory Tech. Rep. LAUR-02-2484, 75 pp.
- Stroeve, J., M. M. Holland, W. Meier, T. Scambos, and M. Serreze, 2007: Arctic sea ice decline: Faster than forecast. *Geophys. Res. Lett.*, **34**, L09501, doi:10.1029/2007GL029703.
- , V. Kattsov, A. Barrett, M. Serreze, T. Pavlova, M. Holland, and W. N. Meier, 2012: Trends in Arctic sea ice extent from CMIP5, CMIP3 and observations. *Geophys. Res. Lett.*, **39**, L16502, doi:10.1029/2012GL052676.

- Thompson, D. W. J., and J. M. Wallace, 1998: The Arctic oscillation signature in the wintertime geopotential height and temperature fields. *Geophys. Res. Lett.*, **25**, 1297–1300, doi:10.1029/98GL00950.
- Timlin, M. S., M. A. Alexander, and C. Deser, 2002: On the reemergence of North Atlantic SST anomalies. *J. Climate*, **15**, 2707–2712, doi:10.1175/1520-0442(2002)015<2707:OTRONA>2.0.CO;2.
- Trenberth, K. E., and J. W. Hurrell, 1994: Decadal atmosphere-ocean variations in the Pacific. *Climate Dyn.*, **9**, 303–319, doi:10.1007/BF00204745.
- Tsukernik, M., C. Deser, M. Alexander, and R. Tomas, 2010: Atmospheric forcing of Fram Strait sea ice export: A closer look. *Climate Dyn.*, **35** (7–8), 1349–1360, doi:10.1007/s00382-009-0647-z.
- Vautard, R., and M. Ghil, 1989: Singular spectrum analysis in nonlinear dynamics, with applications to paleoclimatic time series. *Physica D*, **35**, 395–424, doi:10.1016/0167-2789(89)90077-8.
- von Storch, H., and F. W. Zwiers, 1999: *Statistical Analysis in Climate Research*. Cambridge University Press, 484 pp., doi:10.1017/CBO9780511612336.
- Walsh, J. E., W. L. Chapman, and T. L. Shy, 1996: Recent decrease of sea level pressure in the central Arctic. *J. Climate*, **9**, 480–486, doi:10.1175/1520-0442(1996)009<0480:RDOSLP>2.0.CO;2.
- Wang, J., J. Zhang, E. Watanabe, M. Ikeda, K. Mizobata, J. E. Walsh, X. Bai, and B. Wu, 2009: Is the dipole anomaly a major driver to record lows in Arctic summer sea ice extent? *Geophys. Res. Lett.*, **36**, L05706, doi:10.1029/2008GL036706.
- Watanabe, E., J. Wang, A. Sumi, and H. Hasumi, 2006: Arctic dipole anomaly and its contribution to sea ice export from the Arctic Ocean in the 20th century. *Geophys. Res. Lett.*, **33**, L23703, doi:10.1029/2006GL028112.
- Weng, W., and J. D. Neelin, 1998: On the role of ocean-atmosphere interaction in midlatitude interdecadal variability. *Geophys. Res. Lett.*, **25**, 167–170, doi:10.1029/97GL03507.
- Wettstein, J. J., and C. Deser, 2014: Internal variability in projections of twenty-first-century Arctic sea ice loss: Role of the large-scale atmospheric circulation. *J. Climate*, **27**, 527–550, doi:10.1175/JCLI-D-12-00839.1.
- Wu, B., J. Wang, and J. E. Walsh, 2006: Dipole anomaly in the winter Arctic atmosphere and its association with sea ice motion. *J. Climate*, **19**, 210–225, doi:10.1175/JCLI3619.1.
- Yi, D., L. A. Mysak, and S. A. Venegas, 1999: Decadal-to-interdecadal fluctuations of Arctic sea-ice cover and the atmospheric circulation during 1954–1994. *Atmos.–Ocean*, **37**, 389–415, doi:10.1080/07055900.1999.9649633.
- Zhang, J., M. Steele, D. A. Rothrock, and R. W. Lindsay, 2004: Increasing exchanges at Greenland-Scotland Ridge and their links with the North Atlantic Oscillation and Arctic sea ice. *Geophys. Res. Lett.*, **31**, L09307, doi:10.1029/2003GL019304.